The giant Shakhdara migmatitic gneiss dome, Pamir, India-Asia collision zone: 2. Timing of dome formation

Konstanze Stübner,[1,2] Lothar Ratschbacher,[1] Carsten Weise,[1] Judy Chow,[1] Jakob Hofmann,[1] Jahanzeb Khan,[1] Daniel Rutte,[1] Blanka Sperner,[1] Jörg A. Pfänder,[1] Bradley R. Hacker,[3] István Dunkl,[2] Marion Tichomirowa,[1] M. A. Stearns,[3] and Project TIPAGE members

Received 23 December 2012; revised 21 June 2013; accepted 24 June 2013.

[1] Cenozoic gneiss domes—exposing middle-lower crustal rocks—cover ~30% of the surface exposure of the Pamir, western India-Asia collision zone; they allow an unparalleled view into the deep crust of the Asian plate. We use titanite, monazite, and zircon U/Th-Pb, mica Rb-Sr and $^{40}Ar/^{39}Ar$, zircon and apatite fission track, and zircon (U-Th)/He ages to constrain the exhumation history of the ~350 × 90 km Shakhdara-Alichur dome, southwestern Pamir. Doming started at 21–20 Ma along the Gunt top-to-N normal-shear zone of the northern Shakhdara dome. The bulk of the exhumation occurred by ~NNW-ward extrusion of the footwall of the crustal-scale South Pamir normal-shear zone along the southern Shakhdara dome boundary. Footwall extrusion was active from ~18–15 Ma to ~2 Ma at ~10 mm/yr slip and with vertical exhumation rates of 1–3 mm/yr; it resulted in up to 90 km ~N-S extension, coeval with ~N-S convergence between India and Asia. Erosion rates were 0.3–0.5 mm/yr within the domes and 0.1–0.3 mm/yr in the horst separating the Shakhdara and Alichur domes and in the southeastern Pamir plateau; rates were highest along the dome axis in the southern part of the Shakhdara dome. Incision along the major drainages was up to 1.0 mm/yr. Thermal modeling suggests geothermal gradients as high as 60°C/km along the trace of the South Pamir shear zone and their strong N-S variation across the dome; the gradients relaxed to ≤40–45°C/km since the end of doming.

Citation: Stübner, K., et al. (2013), The giant Shakhdara migmatitic gneiss dome, Pamir, India-Asia collision zone: 2. Timing of dome formation, *Tectonics*, *32*, doi:10.1002/tect.20059.

1. Introduction

[2] The Pamir—the western prolongation of the Tibet-Himalaya orogen—resulted from N-S convergence between India and Asia (Figure 1). In the Pamir, the Cenozoic orogeny formed a high-relief mountain knot of ~500 km N-S extent, which contrasts with the ~1000 km wide, low-relief Tibet Plateau. About ~30% of the surface exposure of the Pamir comprises high-grade, middle to lower crustal metamorphic rocks exhumed in Cenozoic syn-orogenic domes (Figure 1; *Schmidt et al*. [2011], *Stübner et al*. [2013]). Understanding the evolution of these domes is central to understanding the behavior of the Himalaya-Tibet-Pamir orogen because the domes expose a range of shallow to deep structural levels. *Brunel et al*. [1994] and *Robinson et al*. [2004, 2007] explained the formation of the eastern Pamir Muztagh-Ata and Kongur Shan domes by Miocene top-to-S flow and Pliocene/Pleistocene E-W extension, and *Hubbard et al*. [1999], *Schwab et al*. [2004], and *Schmidt et al*. [2011] suggested Miocene formation of the central and southern Pamir domes. In part I of this paper series, *Stübner et al*. [2013] investigated the structural geometry and kinematics of the largest of these Pamir gneiss domes—the 350 × 90 km Shakhdara-Alichur composite gneiss dome in the southwestern Pamir—and established a model of ~N-S extensional doming with footwall exhumation along two low-angle, normal-shear detachments, the South Pamir and Alichur shear zones (SPSZ and ASZ; Figure 2).

[3] Herein, we address the following principal questions: when were the southern Pamir domes formed, and when in particular did ~N-S extension in the southern Pamir start and end? We integrate garnet Lu-Hf [*Smit et al*., 2012]; zircon, monazite, and titanite U/Th-Pb [*Schmidt et al*., 2011; this paper]; mica Rb-Sr and $^{40}Ar/^{39}Ar$; zircon and apatite fission track (AFT); and zircon (U-Th)/He [*Hubbard et al*., 1999; this paper] geo-thermochronology and reconstruct the exhumation history of the Shakhdara-Alichur crystalline rocks.

Additional supporting information may be found in the online version of this article.

[1]Geowissenschaften, TU Bergakademie Freiberg, Freiberg, Germany.
[2]Geowissenschaftliches Zentrum, Universität Göttingen, Göttingen, Germany.
[3]Earth Sciences, University of California, Santa Barbara, California, USA.

Corresponding author: K. Stübner, Geowissenschaften, TU Bergakademie Freiberg, DE-09599 Freiberg, Germany. (konstanze.stuebner@uni-tuebingen.de)

0278-7407/13/10.1002/tect.20059

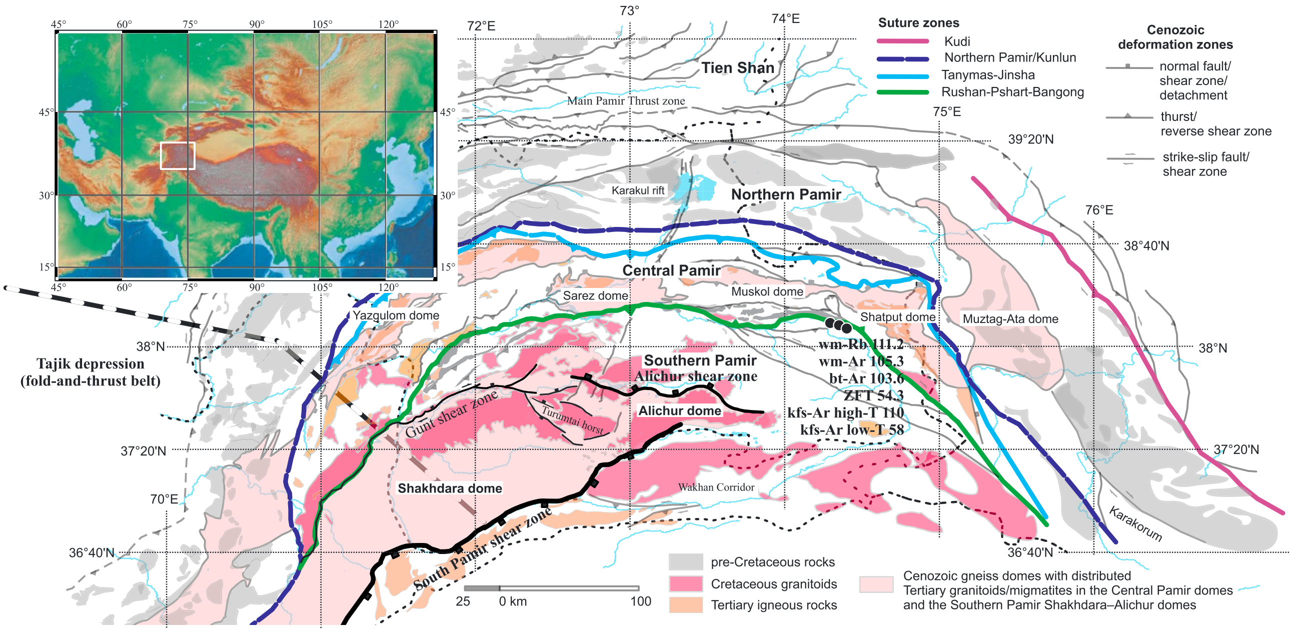

Figure 1. Overview tectonic map of the Pamir showing Phanerozoic sutures and magmatic belts [modified from *Schmidt et al*., 2011]. Outcrops of Cenozoic high-grade, often migmatitic metamorphic rocks in extensional gneiss domes are shown in pink. Digital elevation model in top-left corner locates the Pamir at the northwestern continuation of the Tibet Plateau. Rb-Sr white mica (wm-Rb), $^{40}Ar/^{39}Ar$ white mica, biotite, and K-feldspar (wm-Ar, bt-Ar, kfs-Ar), and zircon fission track (ZFT) ages document cooling of rocks in the southeastern Pamir (see Figures 4 and 5 for the Shakhdara and Alichur dome areas). Dashed line locates the tectonic profile sketch of gneiss-dome formation and foreland accommodation of hinterland extension in Figure 2c.

We conclude that following the India-Asia collision, Eocene-Oligocene crustal shortening with regional migmatization in the late Oligocene-early Miocene was followed by ~N-S extension and exhumation ("doming") since 21–20 Ma; extensional flow continued throughout the Miocene. Flow was continuous from hypersolidus to ductile and brittle-ductile conditions, with cooling ages younging towards the dome-bounding shear zones. Doming ended at ~2 Ma. The domes were affected by up to ~2 km—locally up to 4 km—of erosion, which occurred during and after doming. Earthquake focal-mechanism solutions [*Sippl et al*., 2013] and structural field data [*Stübner et al*., 2013] indicate that deformation has changed dramatically since ~2 Ma to strike-slip shear related to N-S shortening and E-W extension associated with active rifting.

2. Background: Dome Formation by Footwall Exhumation Along Low-Angle Normal-Shear Zones in the Southwestern Pamir

[4] *Grew et al*. [1994], *Robinson et al*. [2004, 2007], *Schmidt et al*. [2011], *Smit et al*. [2012], and *Stübner et al*. [2013] showed that the crystalline rocks of the Pamir domes contain metamorphic mineral assemblages and textures typical of Barrovian facies-series metamorphism, culminating in kyanite + garnet + biotite and migmatites (~750°C, ≥7.5 kbar in the southwestern Pamir) that developed during ~N-S contraction in the Eocene-early Miocene. This prograde metamorphism was followed by syn-tectonic sillimanite or post-tectonic andalusite growth under isothermal decompression during ~N-S stretching.

[5] In the southwestern Pamir, crustal-scale ~N-S extension formed the giant Shakhdara-Alichur composite gneiss dome (Figure 2; *Stübner et al*. [2013]). In the larger Shakhdara dome, middle to lower crustal, partially migmatitic paragneiss and mostly Cretaceous igneous rocks were exhumed by top-to-SSE shear along the ~30° south-dipping SPSZ, which bounds the dome in the south [*Stübner et al*., 2013]. Flow occurred continuously under melt-present to brittle-ductile conditions during progressive exhumation of the crystalline basement rocks and terminated with brittle ~N-S extension. Throughout the dome, the flow plane is subhorizontal, and the flow direction trends ~170°; in the southern Shakhdara dome, the flow plane is warped into a gentle anticline of ~3 km amplitude and ~40 km wavelength (Figure 2). The SPSZ is up to 4 km thick and comprises most of the rocks exposed in the dome. The top of the shear zone is preserved at the highest elevations in the southern dome and constrains the amount of erosion to less than ~2 km (see reconstruction in Figure 2b). The footwall of the SPSZ is exposed along the Panj (Amu Darya) gorge in the "core" of the dome (Figure 2). The northern boundary of the Shakhdara dome comprises a mostly low-grade deformation belt, the Gunt shear/fault zone (GSZ; Figures 1 and 2). There, early top-to- ~N normal to transtensional shear fabrics were folded into a subvertical zone of apparent dextral transpression; this subvertical zone was later overprinted by dextral and normal shear [*Stübner et al*., 2013]. The GSZ separates the zone of ~N-S extension (the Shakhdara dome) from a zone with ~N-S shortening along and above the reactivated

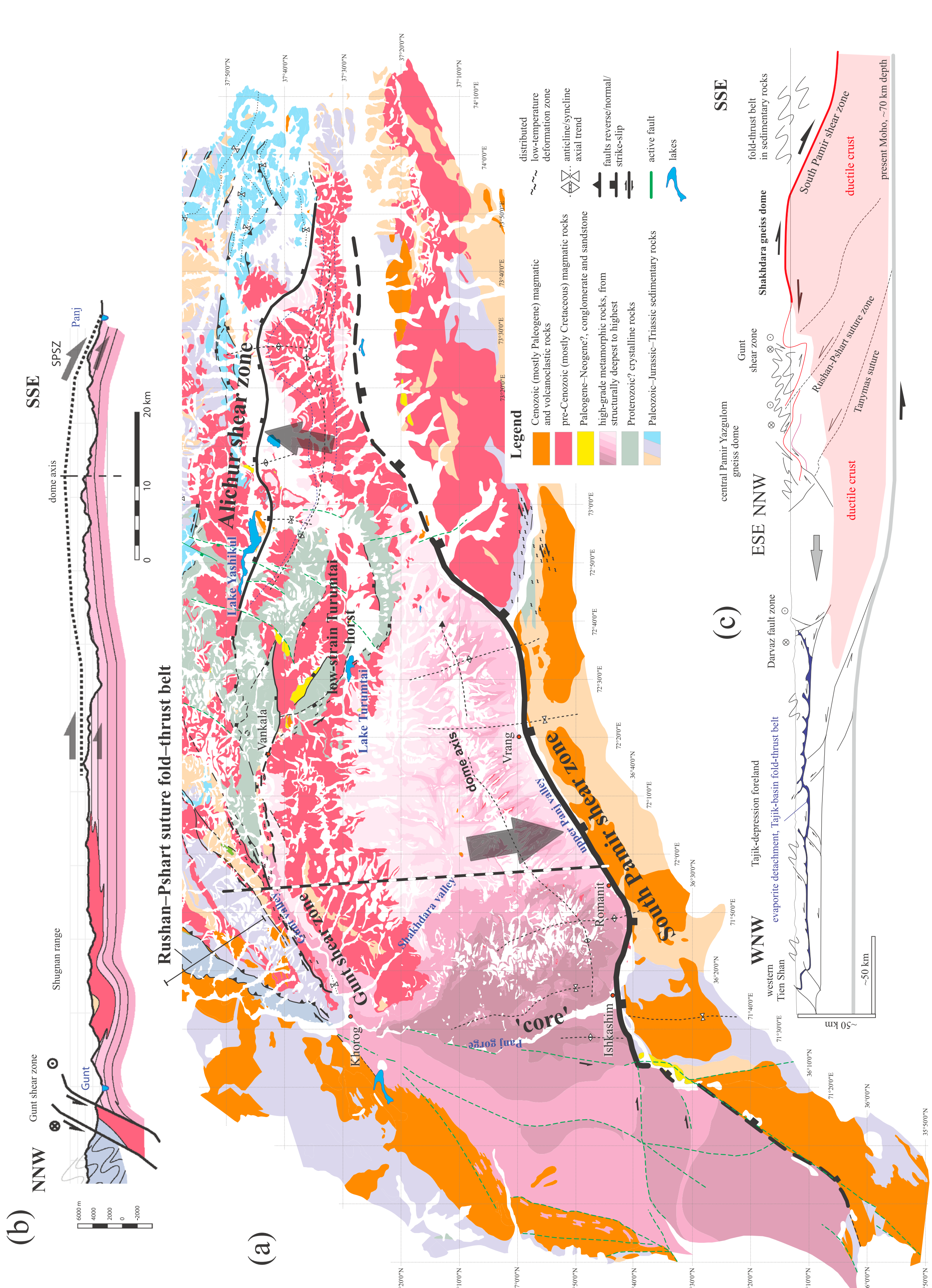
(a)
(b)
(c)
NNW
SSE
Gunt shear zone
Gunt
Shugnan range
dome axis
SPSZ
Panj
20 km
Rushan–Pshart suture fold–thrust belt
Alichur shear zone
South Pamir shear zone
Gunt shear zone
low-strain Turumtai horst
Lake Yashikul
Lake Turumtai
Vankala
Vrang
Romanit
Ishkashim
Khorog
'core'
dome axis
Shakhdara valley
Gunt valley
upper Panj valley
Panj gorge
Legend
Cenozoic (mostly Paleogene) magmatic and volcanoclastic rocks
pre-Cenozoic (mostly Cretaceous) magmatic rocks
Paleogene–Neogene?, conglomerate and sandstone
high-grade metamorphic rocks, from structurally deepest to highest
Proterozoic? crystalline rocks
Paleozoic–Jurassic–Triassic sedimentary rocks
distributed low-temperature deformation zone
anticline/syncline axial trend
faults reverse/normal/ strike-slip
active fault
lakes
WNW
ESE NNW
SSE
western Tien Shan
Tajik-depression foreland
evaporite detachment, Tajik-basin fold-thrust belt
Darvaz fault zone
central Pamir Yazgulom gneiss dome
Gunt shear zone
Shakhdara gneiss dome
fold-thrust belt in sedimentary rocks
South Pamir shear zone
Rushan-Pshart suture zone
Tanymas suture
ductile crust
present Moho, ~70 km depth
~50 km

Figure 2

Rushan-Pshart suture zone north of the domes (Figures 1 and 2).

[6] The smaller Alichur dome consists of Cretaceous orthogneiss/granitoid and is bounded in the north by the ASZ. Deformation is similar to the Shakhdara dome but top-to-N and lower tempered, i.e., rocks exhumed from 10 to 20 km depth [*Stübner et al.*, 2013]. The Shakhdara and Alichur domes are separated by a low-strain, fault segmented horst ("Turumtai horst"; Figure 2). The youngest deformation, contributing little to regional exhumation, is related to active ~E-W graben formation along the meridian axis of the Pamir (Figure 1), and to active strike-slip faults along the northeastern continuation of the Chaman and Herat faults of Pakistan and Afghanistan. Pre- and syn-doming shortening and strike-slip shear, resulting in thick crust (at present ~70 km; *Mechie et al.* [2012] and up to 90 km in the Miocene; *Hacker et al.* [2005]), is locally preserved in the Shakhdara dome and dominates south and north of the domes.

[7] *Stübner et al.* [2013] described the kinematic evolution of the Shakhdara-Alichur domes by footwall exhumation along low-angle detachments, i.e., by a model of metamorphic core-complex formation in extensional tectonic settings. However, this ~N-S extension—as much as 90 km in the Shakhdara dome—occurred within the convergent India-Asia collisional orogen and must have been balanced by contemporaneous crustal shortening. This shortening was accommodated either along and above the reactivated Rushan-Pshart and Tanymas suture zones north(west) of the Shakhdara-Alichur domes or/and within the weak foreland immediately adjacent to the plateau, i.e., within the fold-thrust-belt of the Tajik depression (Figure 1). *Stübner et al.* [2013] suggested that gravitational collapse of thickened southwestern Pamir crust was the driving mechanism for doming and upper-middle crustal extension; collapse drove shortening, in particular in its northwestern foreland, the Tajik depression fold-and-thrust belt. Given the roughly contemporary shortening and extension, this geometry constitutes a ~N-directed "vertical extrusion" channel with frontal and basal underthrusting and thickening and hanging gravitationally driven counterflow.

3. Approach to Timing Dome Formation

[8] We employ high-temperature geochronology [*Schmidt et al.*, 2011; this study] to determine that peak metamorphism and widespread partial melting in the domes (~750°C, ≥7.5 kbar; *Grew et al.* [1994]; *Schmidt et al.* [2011]) occurred in the early Miocene. The exhumation and cooling associated with the onset of extensional doming triggered melt crystallization that is dated by zircon and monazite U/Th-Pb data. Further, the onset of doming is approximated—but, in general, postdated—by the oldest Rb-Sr and $^{40}Ar/^{39}Ar$ cooling ages that show resetting of Cretaceous and older rocks in the Turumtai horst and in the hanging wall of the SPSZ and ASZ detachments.

[9] We assess the timeframe of dome formation and obtain tectonic rates using an extensive titanite U-Pb, mica Rb-Sr and $^{40}Ar/^{39}Ar$, zircon fission track (ZFT), zircon (U-Th)/He (ZHe), and AFT thermochronologic data set. Multithermochronometer data of individual or spatially related samples provide spatially resolved cooling histories. Footwall exhumation along low-angle detachments, as proposed for the Shakhdara and Alichur domes, results—in the absence of erosion—in cooling ages decreasing towards the trace of the detachment. The interpretation of these gradients in terms of onset and end of doming, slip rate along the detachment, and exhumation rate is complicated by the transient nature of the thermal field. Rapid heat advection during the early stages of doming may cause cooling rates to underestimate exhumation rates [e.g., *Turcotte and Schubert*, 2002]; accordingly, cooling-age gradients across the dome may underestimate the slip rate along the detachment. We discuss the effects of heat advection and calculate minimum and maximum tectonic rates (horizontal extension along the shear zones and vertical exhumation).

[10] We further constrain exhumation and the thermal evolution of the Shakhdara dome by elevation profiles. Age-elevation trends result from a combination of tectonic and, especially for low-temperature thermochronometer (herein AFT), erosional exhumation. *Stübner et al.* [2013] reported low-temperature noncoaxial shear along subhorizontal flow planes within the ≤4 km thick SPSZ; this flow may have flattened age-elevation trends of thermochronometers with closure temperatures higher than the deformation temperature. The slope of age-elevation trends may be further reduced by heat advection during exhumation. Therefore, our Rb-Sr, $^{40}Ar/^{39}Ar$, ZFT, and ZHe age-elevation profiles provide minimum exhumation rates. In contrast, thermal relaxation and topographic bending of isotherms cause steepening of age-elevation trends, in particular for low-temperature geochronometers. Herein, we evaluate end-member scenarios to assess exhumation rates.

[11] The youngest cooling ages from the upper- and southernmost part of the SPSZ assess the end of doming. Low-temperature thermochronometers (herein AFT) are affected by rapid erosional or tectonic exhumation. Offsets in cooling

Figure 2. (a) Geologic and structural map of the Shakhdara and Alichur domes and adjacent areas (after *Stübner et al.* [2013], based on *Buchroithner* [1980], *Vlasov et al.* [1991], *Doebrich and Wahl* [2006], and our own fieldwork). Large arrows indicate overall top-to-SSE flow in the Shakhdara and top-to-NNE flow in the Alichur dome. (b) ~N-S profile across the Shakhdara dome (located by dashed line in Figure 2a). The dotted line traces the reconstructed top of the South Pamir shear zone (SPSZ) [from *Stübner et al.*, 2013]. (c) Tectonic profile sketch of gneiss-dome formation in the southwestern Pamir [from *Stübner et al.*, 2013]. The kinematic evolution of the Shakhdara-Alichur domes is characterized by footwall exhumation along low-angle detachments, i.e., by a model of metamorphic core-complex formation in extensional tectonic settings. ~N-S extension is balanced by contemporaneous crustal shortening, which was accommodated in part along and above the reactivated Rushan-Pshart and Tanymas suture zones north(west) of the Shakhdara dome but mostly within the weak foreland immediately adjacent to the plateau, i.e., within the fold-and-thrust belt of the Tajik depression (Figure 1). Gravitational collapse of thickened southwestern Pamir crust was the driving mechanism for doming and upper-middle crustal extension.

Table 1. $^{40}Ar/^{39}Ar$ Data[a]

Sample	Laboratory/ Device	Longitude (E)	Latitude (N)	Altitude (m)	Mineral	Irradiation Parameter (J)	Weight (mg)	Grain Size (μm)	TFA (Ma)	WMA (Ma)
P2s	Stanford/Furnace	73°51.13'	38°07.67'	~3600	Bt	0.0015132	4.6	125–250	98.5 ± 0.6	98.2 ± 0.6
					Kfs-low-T	0.004544	28.8	125–250	91.9 ± 0.9	20.9 ± 0.3
					Kfs-low-T					na
					Kfs-medium-T					na
					Kfs-high-T					99.9 ± 1.0
P5s	Stanford/Furnace	73°34.1’	38° 10.2'	~3560	Bt	0.0015132	1.5	125–250	71.3 ± 0.6	70.0 ± 0.7
					Kfs-very low-T	0.0044590	na		110.6 ± 1.1	58.8 ± 0.6
					Kfs-low-T					
P7s	Stanford/Furnace	74°15.33'	38°11.75'	~3740	Wm	0.001511	0.2	125–250	105.3 ± 1.2	110.0 ± 0.9
					Kfs-low-T	0.0015081	19	125–250	107.4 ±1.1	57.8 ± 0.6
					Kfs-high-T					
4725C1	SEAL/Furnace	74°17.652'	38°10.073'	3699	Bt	0.014376	3.1	63–250	103.6 ± 1.7	103.6 ± 1.7
4726C1	ALF/Laser	72°44.992'	37°29.228'	4206	Bt (1st run)	0.001692	na	80–250	91.5 ± 0.6	119.7 ± 1.0
					Bt (2nd run)	0.0012787	2.29	80–250	87.41 ± 0.97	118.33 ± 0.72
4726D1	SEAL/Furnace	72°43.670'	37°28.586'	3955	Bt	0.014376	3.9	63–250	97.8 ± 2.8	97.7 ± 2.0
4726D1	ALF/Laser				Bt	0.001692	na	80–250	100.99 ± 1.78	104.68 ± 0.33
4726G1	ALF/Laser	72°22.466'	37°41.895'	3174	Bt	0.001692	1.0	80–250	21.61 ± 0.17	21.62 ± 0.22
4726H1	ALF/Furnace	72°14.040'	37°43.068'	3037	Wm	0.001744	0.89	80–250	13.11 ± 0.47	13.11 ± 0.24
4726H1	ALF/Laser				Wm	0.0012787	1.78	80–250	13.24 ± 0.13	12.92 ± 0.11
4726H1	ALF/Laser				Bt	0.001692	2.87	80–250	13.46 ± 0.12	13.31 ± 0.08
4726H1	ALF/Laser				Bt	0.0012787	2.14	80–250	11.75 ± 0.12	11.88 ± 0.11
6821A1	ALF/Laser	71°50.161'	36°46.608'	4260	Bt	0.0012787	2.37	80–250	9.68 ± 0.14	10.02 ± 0.01
6821P2	ALF/Laser	71°51.2377'	36°46.0775'	3997	Bt	0.0043158	2.66	80–250	12.25 ± 0.24	12.42 ± 0.24
6822A3	ALF/Laser	71°56.102'	36°44.974'	2671	Wm	0.0012332	2.11	80–250	5.90 ± 0.12	6.12 ± 0.12
6822R1	ALF/Laser	71°42.470'	36°40.535'	2565	Bt	0.00436345	3.25	80–250	18.49 ± 0.13	18.79 ± 0.10
6822T1	ALF/Laser	71°44.4203'	36°40.4299'	2582	Bt	0.00436345	2.64	80–250	16.57 ± 0.13	16.56 ± 0.07
6822W1	ALF/Laser	71°43.9401'	36°40.4527'	2558	Wm	0.0043635	2.27	80–250	16.05 ± 0.30	15.93 ± 0.21
					Bt	0.00436345	2.44	80–250	14.82 ± 0.15	15.78 ± 0.21
6822X1	ALF/Furnace	71°45.711'	36°40.699'	2597	Wm	0.001806	11.4	80–250	15.09 ± 0.05	15.24 ± 0.03
6823A3	ALF/Laser	71°54.432'	36°44.441'	2696	Bt	0.00436345	2.33	80–250	8.30 ± 0.12	7.90 ± 0.37
6823C1	ALF/Laser	71°32.376'	36°51.212'	2464	Bt	0.0012787	2.68	80–250	5.96 ± 0.17	6.15 ± 0.12
6824B1	ALF/Laser	71°32.126'	37°05.033'	4603	Bt-high-T	0.0012332	2.91	80–250	9.90 ± 0.05	12.42 ± 0.08
					Bt-low-T					10.98 ± 0.28
6824B4	ALF/Laser	71°32.126'	37°05.033'	4603	Bt	0.0012332	3.01	80–250	9.76 ± 0.10	10.51 ± 0.09
6824D1	ALF/Laser	71°32.141'	37°04.694'	4299	Bt-high-T	0.0012332	4.19	80–250	7.66 ± 0.15	9.57 ± 0.1
					Bt-low-T					6.15 ± 0.25
6824E1	ALF/Laser	71°32.268'	37°04.594'	4096	Bt	0.0012332	1.76	80–250	8.98 ± 0.16	9.55 ± 0.12
6824F1	ALF/Laser	71°32.349'	37°04.382'	3847	Bt	0.0012332	2.75	80–250	8.62 ± 0.12	8.87 ± 0.07
6825B1	ALF/Laser	71°29.019'	37°01.740'	2507	Bt	0.0012332	2.1	80–250	14.36 ± 0.15	14.57 ± 0.15
6825D1	ALF/Furnace	71°28.066'	37°10.720'	2785	Wm	0.001806	16.1	80–250	10.88 ± 0.05	11.02 ± 0.03
6826D1	ALF/Furnace	71°43.044'	37°19.982'	2585	Wm	0.001806	11.5	80–250	12.74 ± 0.06	12.81 ± 0.03
					Bt	0.001806	na	80–250	12.98 ± 0.05	13.23 ± 0.05
6827A2	ALF/Laser	71°38.987'	37°23.869'	2383	Wm	0.0043158	2.73	80–250	9.65 ± 0.08	9.60 ± 0.09
					Bt	0.0012332	4.97	80–250	12.99 ± 0.07	13.30 ± 0.25
6829A1	ALF/Laser	71°46.422'	37°10.279'	3706	Bt	0.00436345	2.87	80–250	10.52 ± 0.13	10.93 ± 0.08

Table 1. $^{40}Ar/^{39}Ar$ Data[a]

IIA (Ma)	MSWD (of IIA)	$^{40}Ar/^{36}Ar$	%^{39} Ar	Steps (Total Number)	Interpretation Age (± 2σ)	Cooling Rate (°C/Myr)	Closure Temperature (°C)
98.3 ± 0.7	4.0	295 ± 5	99	na	98.2 ± 0.6 Ma; published by Schwab et al. [2004]	3	330
20.0 ± 1.5	4.1	315 ± 28	1	na			
24.5 ± 0.5	1.6	426 ± 8	2	na	22 ± 2 Ma	3	300 ± 50
22.3 ± 1.9	1.9	931 ± 52	3	na			
99.0 ± 1.1	4.7	325 ± 12	58	na	99.0 ± 1.1 Ma	3	300 ± 50
qualitative multidomain interpretation: rapid cooling through >300°C at ~99 Ma, reheating through ~200°C at ~22 Ma							
69.7 ± 1	5.0	284 ± 5	82	na	70.0 ± 0.7 Ma; published by Schwab et al. [2004]	3	330
59.3 ± 0.7	0.02	285 ± 5	2	na	59 ± 3 Ma, reheating	3	300 ± 50
68.3 ± 2.2	1.5	2649 ± 483	21	na	68 ± 5 Ma, rapid cooling	3	300 ± 50
qualitative multidomain interpretation: rapid cooling through >300°C at ~68 Ma, reheating through ~200°C at ~59 Ma							
100.9 ± 6.0	4.4	266 ± 15	100	na	105.3 ± 1.2 Ma; published by Schwab et al. [2004]	3	359
57.9 ± 0.7	21.0	282. ± 12	2	na	58 ± 2 Ma, reheating	3	300 ± 50
110.7 ± 3.0	147	895 ± 215	53	na	110 ± 5 Ma, initial cooling	3	300 ± 50
qualitative multidomain interpretation: rapid cooling through >300°C at ~110 Ma, reheating through ~200°C at ~58 Ma							
104.0 ± 1.3	1.5	303 ± 30	72	na	103.6 ± 1.7 Ma	3	330
105 ± 37	0.04	490 ± 480	36	6–8 (14)	119 ± 4 Ma; loss profile to ~25 Ma	2	324
118 ± 26	0.007	297 ± 380	31	7–12 (17)	118 ± 2 Ma; loss profile to <23 Ma	2	324
98.6 ± 3.0	0.1	289 ± 140	38	na	98 ± 4 Ma } 104 ± 3 Ma	2	324
105.1 ± 3.9	0.35	280 ± 130	41	14–16 (21)	104. 5 ± 3.0 Ma		
21.63 ± 0.46	0.25	295 ± 2	98	2–18 (18)	21.62 ± 0.50 Ma	10	348
12.9 ± 1.5	0.19	307 ± 63	100	1–14 (14)	13.0 ± 0.5 Ma } 13.0 ± 0.5 Ma	40	407
14.4 ± 3.1	0.17	188 ± 210	69	na	13.0 ± 0.5 Ma		
13.27 ± 0.27	0.11	296 ± 2	99	2–19 (19)	13.3 ± 0.3 Ma } 12.5 ± 1.0 Ma	40	370
11.79 ± 0.46	0.29	298 ± 8	84	3–14 (17)	11.8 ± 0.2 Ma		
10.00 ± 0.35	0.62	292 ± 7	100	1–24 (24)	10.0 ± 0.2 Ma	60	377
12.41 ± 0.32	2.0	298 ± 9	88.7	6–17 (20	12.4 ± 1.0 Ma	60	377
6.09 ± 0.59	0.69	295 ± 16	83	2–14 (17)	6.1 ± 0.5 Ma	60	416
18.95 ± 0.29	0.20	280 ± 29	85.7	6–13 (16)	18.85 ± 0.20 Ma	20	359
16.64 ± 0.26	0.07	294 ± 6	95.9	4–16 (18)	16.6 ± 0.1 Ma	20	359
13.1 ± 2.5	0.07	566 ± 830	63.5	11–21 (29)	15.9 ± 0.5 Ma	20	394
15.99 ± 0.42	0.47	283 ± 24	71.5	6–13 (16)	15.8 ± 0.2 Ma; two steps at 3.2 ± 2.8 Ma	20	359
15.03 ± 0.18	1.7	293 ± 31	98.1	6–27 (29)	15.2 ± 0.3 Ma, two steps at 7.3 ± 1.9 Ma	20	394
8.06 ± 0.52	0.60	293 ± 6	36.5	5–9 (14)	8.0 ± 1.0 Ma, two steps at 10.32 ± 0.21 Ma	60	377
6.15 ± 0.48	0.51	289 ± 19	95.6	6–24 (25)	6.15 ± 0.20 Ma	50	374
12.49 ± 0.66	0.72	292 ± 24	60	21–26 (27)	12.45 ± 0.15 Ma, high-T plateau	50	374
11.02 ± 0.81	0.24	295 ± 5	32	2–19 (27)	11.0 ± 0.5 Ma, low-T plateau	50	374
9.49 ± 0.53	2.5	306 ± 6	79.6	11–26 (27)	10 ± 1 Ma; loss profile to ~4.6 Ma	50	374
10.6 ± 1.6	0.07	213 ± 120	37	23–26 (27)	10 ± 1 Ma; oldest step ~13.5 Ma	50	374
6.34 ± 0.74	0.46	293 ± 7	43	4–20 (27)	6.3 ± 0.5 Ma		
9.71 ± 0.79	0.21	289 ± 27	79	9–17 (18)	9.6 ± 0.5 Ma; loss profile to 4.6 ± 2.5 Ma	50	374
8.95 ± 0.26	0.19	291 ± 7	95	4–16 (17)	8.9 ± 0.1 Ma, loss to ~5 Ma	50	374
15.01 ± 0.90	0.37	287 ± 14	87	5–17 (17)	15.0 ± 0.5 Ma	50	374
11.04 ± 0.10	0.44	296 ± 1	97	10–25 (26)	11.03 ± 0.10 Ma	50	412
12.81 ± 0.21	0.97	295 ± 6	98	4–22 (25)	12.8 ± 0.2 Ma; loss profile to 6.2 ± 3.9 Ma	40	407
13.21 ± 0.36	1.9	302 ± 24	95	6–12 (13)	13.3 ± 0.3 Ma; loss profile to < 8 Ma	40	370
9.71 ± 0.36	0.37	288 ± 25	99.7	3–18 (19)	9.7 ± 0.5 Ma	40	407
13.30 ± 0.25	0.25	293 ± 3	85	3–29 (31)	13.30 ± 0.25 Ma	40	370
10.94 ± 0.25	0.17	296 ± 10	91.7	7–24 (25)	10.93 ± 0.04 Ma	40	370

Table 1. (continued)

Sample	Laboratory/ Device	Longitude (E)	Latitude (N)	Altitude (m)	Mineral	Irradiation Parameter (J)	Weight (mg)	Grain Size (μm)	TFA (Ma)	WMA (Ma)
6829B1	ALF/Furnace	71°44.851'	37°08.633'	4372	Bt	0.001806	2.2	80–250	12.03 ± 0.06	12.08 ± 0.37
6829C1	ALF/Furnace	71°45.586'	37°09.637'	4014	Bt	0.001806	7.7	80–250	12.05 ± 0.15	12.04 ± 0.04
6831A1	ALF/Laser	72°07.206'	37°13.466'	3045	Wm	0.0043635	2.27	80–250	15.28 ± 0.15	15.16 ± 0.08
6831C3	ALF/Furnace	72°11.363'	37°14.504'	3104	Bt	0.001806	1.0	80–250	9.90 ± 0.05	10.05 ± 0.04
6901B1	ALF/Laser	72°33.751'	37°20.574'	3702	Bt	0.0012787	3.08	80–250	10.28 ± 0.09	10.39 ± 0.07
6901C1	ALF/Laser	72°34.929'	37°24.534'	4060	Wm	0.0012332	2.19	80–250	12.94 ± 0.09	13.09 ± 0.06
6901E1	ALF/Furnace	72°39.503'	37°33.429'	3716	Bt	0.001806	1.0	80–250	100.22 ± 1.39	100.88 ± 0.52
6902C1	ALF/Laser	72°22.923'	37°39.976'	4045	Wm	0.0043158	2.48	80–250	30.46 ± 0.11	30.46 ± 0.11
6903D2	ALF/Furnace	72°14.424'	37°42.935'	3032	Bt	0.001806	1.1	80–250	12.27 ± 0.08	12.96 ± 0.06
6904M1	ALF/Laser	71°44.707'	37°37.817'	3077	Wm	0.0012787	1.58	80–250	16.31 ± 0.13	16.53 ± 0.01
6904P2	ALF/Laser	71°44.688'	37°38.397'	3543	Bt	0.0012787	2.39	80–250	17.94 ± 0.12	18.11 ± 0.10
6904Q3	ALF/Laser	71°44.9793'	37°37.3207'	2850	Wm	0.0043158	2.28	80–250	15.26 ± 0.11	15.16 ± 0.09
					Bt	0.00436345	2.5	80–250	13.84 ± 0.10	14.13 ± 0.11
6905B1	ALF/Laser	71°45.218'	37°36.825'	3412	Wm	0.0043158	2.61	80–250	13.67 ± 0.18	13.76 ± 0.10
					Bt	0.00436345	2.5	80–250	12.49 ± 0.14	12.88 ± 0.13
6905C2	ALF/Furnace	71°30.323'	37°32.382'	2780	Wm	0.00097415	1.0	80–250	16.39 ± 0.19	15.53 ± 0.21
					Bt	0.00806	2.2	80–250	15.86 ± 0.52	16.07 ± 0.09
996A1	ALF/Laser	71°41.182'	36°40.95'	2606	Wm	0.004227	2.16	80–250	19.60 ± 0.11	19.62 ± 0.18
996B1	ALF/Laser	71°43.9266'	36°41.553'	2750	Bt	0.0043635	2.48	80–250	8.92 ± 0.12	8.64 ± 0.07
996B2	ALF/Laser	71°44.4144'	36°40.9056'	2639	Bt	0.0043158	2.96	80–250	18.43 ± 0.08	18.25 ± 0.25
997A2	ALF/Laser	72°10.46'	36°54.82'	2810	Bt	0.00436345	2.63	80–250	5.07 ± 0.14	5.17 ± 0.09
998E1	ALF/Laser	72°15.2017'	37°02.16'	4154	Bt	0.00436345	2.56	80–250	8.20 ± 0.18	7.90 ± 0.05
999B5	ALF/Laser	72°15.5633'	36°58.4633'	3183	Bt	0.0043635	2.52	80–250	5.49 ± 0.14	5.51 ± 0.08
999H1	ALF/Laser	72°32.8333'	37°00.2117'	2819	Bt	0.0043635	2.34	80–250	4.40 ± 0.88	5.46 ± 0.06
9910A1	ALF/Laser	72°42.74'	37°05.9033'	3285	Bt	0.0043635	2.72	80–250	6.40 ± 0.10	6.39 ± 0.08
9916G6	ALF/Laser	72°57.3167'	37°54.2017'	4401	Bt	0.0043158	2.62	80–250	15.57 ± 0.10	15.67 ± 0.06

Table 1. (continued)

IIA (Ma)	MSWD (of IIA)	$^{40}Ar/^{36}Ar$	$\%^{39}$ Ar	Steps (Total Number)	Interpretation Age (± 2σ)	Cooling Rate (°C/Myr)	Closure Temperature (°C)
11.98 ± 0.56	12	295 ± 12	97	3–13 (15)	12.0 ± 0.7 Ma	40	370
12.04 ± 0.19	4.0	299.6 ± 4.1	96	4–18 (18)	12.0 ± 0.5 Ma	40	370
15.2 ± 1.2	0.087	295 ± 45	95.2	5–28(29)	15.2 ± 0.1 Ma	40	407
10.06 ± 0.11	0.29	295 ± 2	98	6–13 (13)	10.0 ± 0.1 Ma; loss profile to <7 Ma	40	370
10.29 ± 0.30	0.40	300 ± 9	98	3–24 (25)	10.3 ± 0.2 Ma	40	370
13.76 ± 0.74	0.38	252 ± 45	98	4–17 (17)	13.2 ±0.5 Ma	40	407
101.9 ± 1.8	2.6	236 ± 120	90	6–16 (19)	101.0 ± 1.5 Ma, two steps at 41.9 ± 2.0 Ma	2	324
30.6 ± 1.2	0.16	294 ± 38	100	1–30(30)	30.5 ± 0.1 Ma	10	381
12.98 ± 0.15	0.37	293 ± 4	89	5–15 (16)	12.97 ± 0.15 Ma	40	370
16.82 ± 0.89	0.77	283 ± 31	99	na	16.6 ± 0.3 Ma	40	407
18.18 ± 0.45	0.27	295 ± 6	99	3–24 (25)	18.15 ± 0.15 Ma	40	370
14.97 ± 0.46	0.12	361 ± 100	97.9	4–29(29)	15.1 ± 0.1 Ma	40	407
14.23 ± 0.25	0.39	293 ± 7	94.0	5–24 (26)	14.2 ± 0.2 Ma	40	370
13.72 ± 0.82	0.091	308 99	96.7	4–32 (33)	13.75 ± 0.20 Ma	40	407
13.25 ± 0.64	0.19	281 ± 24	85.8	6–25 (26)	13.0 ± 0.3 Ma	40	370
15.52 ± 0.32	0.65	299 ± 9	58.7	1–22 (36)	15.5 ± 0.5 Ma	40	407
16.11 ± 0.26	0.18	293 ± 9	86	1–6 (12)	16.1 ± 1.0 Ma	40	370
19.45 ± 0.33	0.47	309 ± 13	97.9	4–19 (19)	19.5 ± 0.3 Ma	20	394
8.51 ± 0.48	0.099	320 ± 66	85.9	8–22 (26)	8.6 ± 0.1 Ma	60	377
18.33 ± 0.52	2.9	291 ± 63	88.9	6–20 (21)	18.25 ± 0.50 Ma	20	359
5.19 ± 0.26	0.20	293 ± 38	97.8	4–24 (26)	5.18 ± 0.10 Ma	60	377
7.94 ± 0.40	0.041	288 ± 82	89.7	13–33(33)	7.9 ± 0.1 Ma	60	377
5.48 ± 0.26	0.13	300 17	90.9	6–24 (26)	5.5 ± 0.1 Ma	60	377
5.46 ± 0.30	0.045	296 ± 3	77.4	5–16 (23)	5.46 ± 0.10 Ma	60	377
6.36 ± 0.19	0.23	299 ± 11	94.6	8–23 (26)	6.39 ± 0.1 Ma	60	377
15.70 ± 0.20	0.15	296 ± 4	99.3	4–18 (18)	15.7 ± 0.1 Ma	20	359

[a]TFA, total gas age; WMA, weighted mean age; IIA, inverse isochron age; errors are 2 σ; MSWD, mean square weighted deviation, which expresses the goodness of fit of the isochron; isochron and weighted mean ages are based on fraction of ^{39}Ar and steps listed. Wm, white mica; Kfs, potassium feldspar; Bt, biotite; low-T, low-temperature steps; medium-T, intermediate-temperature steps; high-T, high-temperature steps; na, not applicable or analyzed. Stanford, SEAL, ALF, Ar-laboratories at Stanford University, USA, Slovak Academy of Sciences, Bratislava, Slovakia, and TU Bergakademie, Freiberg, Germany. See Figure S2 and Table S3 for analytical data and graphical representation. Cooling rates stem from multiple thermochronometer data that were obtained from the sample location. Closure temperatures are calculates with the program CLOSURE [*Brandon et al.*, 1998].

Table 2. Zircon Fission Track Data[a]

Sample	Areas	N_s	N_i	χ^2	$P(\chi^2)$	$\zeta \pm 1\sigma$	$\rho_d \pm 1\sigma$ [10^6 cm^{-2}]	Sample Age ± 1σ [Ma]	Cooling Rate [°C/Myr]	T_c [°C]
6829B1	26	3939	4579	55.30	0.04	101.6 ± 2.0	1.911 ± 0.078	8.3 ± 0.4	40	351
6822E1	23	1518	2684	75.20	0.00	101.6 ± 2.0	1.919 ± 0.077	5.5 ± 0.3	60	355
6904G1	22	2688	954	100.25	0.00	101.6 ± 2.0	1.928 ± 0.077	27.5 ± 1.6	10	338
6824B4	27	6752	5432	260.21	0.00	101.6 ± 2.0	1.945 ± 0.083	12.3 ± 0.6	50	353
P5s	21	2370	550	52.94	0.01	101.6 ± 2.0	1.951 ± 0.086	42.6 ± 2.9	3	327
6901D1	20	6553	1671	102.47	0.00	101.6 ± 2.0	1.966 ± 0.101	39.1 ± 2.4	2	324
M96A7	20	3619	659	207.46	0.00	101.6 ± 2.0	1.954 ± 0.093	54.3 ± 3.6	3	327
6824E1	23	1137	1207	47.00	0.15	101.6 ± 2.0	1.914 ± 0.078	9.2 ± 0.6	50	353

[a]N_s, N_i: number of spontaneous, induced tracks; ρ_d: induced track density from glas standard, extrapolated to the respective position of the mount within the irradiation batch. All ages are pooled ζ-ages. T_c: closure temperature [*Dodson*, 1973], calculated with software Closure [*Brandon et al.*, 1998], based on fanning model of *Tagami et al.* [1998].

ages of particular thermochronometers, for example across the SPSZ, may result from differential exhumation, implying a primary control of the cooling ages in the footwall by tectonic exhumation; alternatively, the age offset may result from high post-tectonic erosion rates affecting a hot footwall and a relatively cool hanging wall. Estimating the amount of syn- and post-tectonic erosion and its spatial variation is therefore essential to constrain the end of dome formation. We estimated the amount of erosion from profiles across the domes [*Stübner et al.*, 2013].

4. Results

[12] Appendices A1–A5 summarize the sample-preparation methodology and the geo-thermochronologic methods employed in this study. Tables 1–4 list the Rb-Sr, ^{40}Ar/^{39}Ar, ZFT, ZHe, and AFT ages. Figures S1 and S2 of the supporting information display our new U-Pb titanite and ^{40}Ar/^{39}Ar and Rb-Sr mica data. Tables S1 to S4 of the supporting information provide sample locations and descriptions, and the analytical details of the U-Pb titanite, ^{40}Ar/^{39}Ar mica, and Rb-Sr mica studies.

[13] In the following, we use regionally distributed geo-thermochronologic data to establish the age of formation and exhumation of the composite Shakhdara-Alichur dome and to derive first-order cooling, slip, and exhumation rates. For this, we rely on the horizontal and vertical distributions of ages, cooling rates estimated from multiple thermochronometers, and exhumation rates approximated from age-elevation relationships. Detailed interpretation of our new geo-thermochronology in terms of petrophysical parameters and relationships to structures (e.g., mineral chemistry; grain-size variation in heterogeneously deformed rocks and in relation to dynamic/static recrystallization; mineral formation relative to petrologically determined pressure-temperature paths) is the subject of a forthcoming paper in this series. For multiple thermochronometer cooling-rate studies, we employed the closure-temperature concept [*Dodson*, 1973]. For the Rb-Sr system, we used whole-grain closure temperatures of 550 ± 30°C and 350 ± 30°C for white mica and biotite, respectively [*Jenkin*, 1997]. For the ^{40}Ar/^{39}Ar system, we calculated closure temperatures for white mica (Wm) and biotite (Bt) with the program CLOSURE [*Brandon et al.*, 1998] and typically obtained 360–380°C (Bt) and 400–420°C (Wm), and 330–340°C and 360–380°C for rapidly and more slowly cooled samples, respectively (Table 1). Similar calculations for ZFT, ZHe, and AFT yielded closure-temperature ranges of 360–330°C, 210–170°C, and 140–110°C, respectively; Tables 2–4 give the temperatures for each sample. Appendices A2–A4 provide the details of the calculations and the parameters appropriate for the southern Pamir.

[14] Figure 3 provides an overview of the geo-thermochronologic database from the Shakhdara and Alichur domes, displayed as kernel-density estimate curves, probability density plots, and histograms (see *Vermeesch* [2012] for definitions and implementation). Garnet Lu-Hf ages cluster at ~37 Ma [*Smit et al.*, 2012]. Th-Pb single-grain monazite ages show two clusters at ~28 and ~21 Ma. The younger cluster is from migmatitic para- and orthogneiss and is identical with metamorphic zircons from leucocratic pegmatite [*Schmidt et al.*, 2011]; the older cluster mostly comprises data from paragneiss of the southeastern margin of the Shakhdara dome where migmatitic features are rare. Our new titanite U-Pb data (Figure S1) include two ages at ~21 Ma from deformed pegmatite along the northern rim of the Shakhdara dome and restite in leucosome from the very top of the SPSZ. Five additional samples from an elevation profile in the core of the Shakhdara dome span 15 to 11 Ma. Mica Rb-Sr and ^{40}Ar/^{39}Ar ages are broadly distributed, with a median at ~12 Ma (Figure 3). All ZFT ages older than ~12 Ma are from samples outside the Shakhdara dome, i.e., the Turumtai horst, the hanging wall of the Alichur dome, or the SE Pamir. Similarly, ZHe ages within the dome are younger than ~9 Ma, and older ages come from the Turumtai horst and from north of the domes. AFT ages are broadly distributed and centered at ~6 Ma. Regressions through the peak ages of the clusters of these geo-thermochronometers and the corresponding means of their closure temperatures for single samples yielded bulk cooling rates of 40 to 83°C/Ma, depending on whether monazite or titanite is excluded from the regression (Figure 3).

[15] Figures 4 to 6 are simplified structural maps showing the spatial distributions of the cooling ages. In the Shakhdara-dome crystalline rocks, most of the Rb-Sr and ^{40}Ar/^{39}Ar mica ages are Miocene (20–4 Ma; Figure 4); only one sample along its northern margin yielded an older Rb-Sr Wm age (24.9 Ma). The youngest ages occur along the SPSZ (~8–5 Ma), the oldest ones along the northern rim of the dome (~18–13 Ma) and within the southern hanging wall (~20–15 Ma; Figure 4 inset). This is in agreement with the ZFT ages (Figure 5): three samples from the central dome are 12.3–8.3 Ma, and sample 6822E1 from the SPSZ is 5.5 ± 0.6 Ma. ZHe ages (Figure 5) are generally younger than the ^{40}Ar/^{39}Ar and ZFT ages and also young southward from the northern Shakhdara rim (16.8–9.3 Ma) to the SPSZ

Table 3. Zircon (U-Th)/He Data[a]

Sample	aliq.	He vol. [ncc]	He 1σ [%]	U238 mass [ng]	U238 1σ [%]	Th232 mass [ng]	Th232 1σ [%]	Th/U ratio	Sm mass [ng]	Sm 1σ [%]	Ejection Correct. (Ft)	Uncorr. He-age [Ma]	Ft-Corr. He-age [Ma]	2σ [Ma]	Sample Unweighted Aver. age [Ma]	±2 s.e. [Ma]	Equiv. sphere Radius [μm]	Cooling Rate [°C/Myr]	Closure Temperature [°C]
4726B1	z1	5.99	1.74	5.46	1.8	0.09	2.4	0.02	0.01	8.5	0.773	9.04	11.70	0.98	11.7	0.6	52	50	196
	z2	3.01	1.82	3.11	1.8	0.14	2.4	0.04	0.01	8.5	0.745	7.95	10.67	0.98					
	z3	6.15	1.73	5.15	1.8	0.13	2.4	0.02	0.01	7.4	0.774	9.82	12.69	1.06					
4726H2	z1	2.24	1.88	3.28	1.8	0.84	2.4	0.26	0.02	5.8	0.737	5.33	7.23	0.68	7.2	0.4	49	40	193
	z2	2.44	1.86	3.71	1.8	1.33	2.4	0.36	0.05	4.5	0.772	5.03	6.51	0.55					
	z3	3.32	1.82	4.51	1.8	0.76	2.4	0.17	0.02	7.5	0.743	5.86	7.89	0.72					
6821A1	z1	1.53	1.82	3.73	1.8	2.06	2.4	0.55	0.17	5.7	0.846	3.01	3.56	0.24	3.7	0.1	80	60	207
	z2	2.03	1.78	4.50	1.8	2.51	2.4	0.56	0.35	5.9	0.847	3.29	3.89	0.26					
	z3	2.38	1.77	5.16	1.8	3.05	2.4	0.59	0.34	5.9	0.837	3.35	4.00	0.27					
	z4	2.01	1.85	5.00	1.8	2.77	2.4	0.55	0.21	10.8	0.837	2.94	3.51	0.24					
6822E1	z1	0.72	1.99	3.09	1.8	0.53	2.4	0.17	0.04	20.9	0.811	1.86	2.29	0.18	2.7	0.2	66	60	203
	z2	1.79	1.80	5.73	1.8	1.10	2.4	0.19	0.06	20.8	0.805	2.48	3.08	0.24					
	z3	1.60	1.81	5.60	1.8	1.23	2.4	0.22	0.06	21.0	0.818	2.25	2.75	0.20					
6824F1	z1	1.87	1.8	2.50	1.8	0.93	2.4	0.37	0.03	12.9	0.819	5.68	6.93	0.50	7.5	0.4	72	50	203
	z2	1.77	1.8	2.34	1.8	0.99	2.4	0.42	0.07	12.7	0.829	5.68	6.85	0.48					
	z3	1.11	1.9	1.25	1.8	0.55	2.4	0.44	0.18	12.6	0.813	6.67	8.20	0.62					
	z4	1.53	1.9	1.93	1.8	1.21	2.4	0.63	0.03	12.8	0.841	5.71	6.79	0.46					
	z5	1.15	1.8	1.18	1.8	0.63	2.4	0.53	0.04	12.8	0.793	7.21	9.08	0.72					
	z6	1.07	1.9	1.27	1.8	0.76	2.4	0.60	0.06	12.7	0.801	6.12	7.63	0.58					
	z7	1.91	1.8	1.84	1.8	1.18	2.4	0.64	0.04	12.9	0.826	7.45	9.02	0.64					
	z8[b]	4.11[b]	1.7[b]	0.61[b]	1.8[b]	2.77[b]	2.4[b]	4.55[b]	0.28[b]	12.7[b]	0.835[b]	26.76[b]	32.03[b]	2.16[b]					
	z9	2.45	1.8	4.55	1.8	2.74	2.4	0.60	0.13	12.7	0.844	3.91	4.63	1.00					
	z10	2.46	1.7	3.08	1.8	1.72	2.4	0.56	0.08	12.7	0.825	5.84	7.08	0.50					
	z11	4.60	1.7	5.22	1.8	3.00	2.4	0.57	0.07	12.7	0.861	6.43	7.47	0.46					
	z12	1.78	1.8	2.27	1.8	1.06	2.4	0.47	0.16	12.7	0.827	5.83	7.06	0.50					
	z13	2.15	1.8	2.16	1.8	1.45	2.4	0.67	0.08	12.7	0.808	7.13	8.83	0.66					
6829C1	z1	19.61	1.66	20.46	1.8	3.33	2.4	0.16	0.03	6.7	0.864	7.64	8.85	0.55	8.7	0.3	91	40	206
	z2	8.23	1.69	9.58	1.8	1.45	2.4	0.15	0.03	7.3	0.858	6.87	8.01	0.51					
	z3	11.76	1.68	11.77	1.8	2.29	2.4	0.20	0.10	6.2	0.866	7.92	9.14	0.57					
6831C1	z1	3.90	1.72	5.78	1.8	0.89	2.4	0.15	0.00	11.8	0.805	5.40	6.71	0.51	6.8	0.5	62	40	198
	z2	14.26	1.66	18.00	1.8	6.23	2.4	0.35	0.04	6.7	0.808	6.07	7.51	0.55					
	z3	9.30	1.67	11.60	1.8	4.82	2.4	0.42	0.02	7.5	0.800	6.04	7.55	0.57					
	z4	0.66	2.14	1.18	1.8	0.69	2.4	0.59	0.04	11.5	0.779	4.09	5.25	0.44					
6901E1	z1	55.13	1.64	20.01	1.8	5.98	2.4	0.30	0.15	19.1	0.842	21.29	25.30	1.68	25.8	2.9	82	10	189
	z2	20.77	1.65	8.93	1.8	2.58	2.4	0.29	0.38	19.2	0.857	18.01	21.01	1.33					
	z4	26.39	1.65	7.87	1.8	1.91	2.4	0.24	0.04	19.8	0.841	26.21	31.18	2.08					
6902G1	z1	20.05	1.65	14.80	1.8	10.98	2.4	0.74	0.12	6.5	0.820	9.54	11.64	0.82	13.7	1.2	73	10	187
	z2	21.60	1.65	12.09	1.8	5.61	2.4	0.46	0.06	6.7	0.837	13.32	15.92	1.07					
	z3	18.83	1.65	12.16	1.8	7.61	2.4	0.63	0.16	6.0	0.823	11.17	13.56	0.95					
6903B1	z1	6.66	1.69	5.73	1.8	0.70	2.4	0.12	0.02	9.4	0.792	9.35	11.81	0.93	11.4	0.3	55	10	181
	z2	4.37	1.71	3.98	1.8	0.28	2.4	0.07	0.01	12.6	0.766	8.94	11.66	0.99					
	z3	5.40	1.69	5.25	1.8	0.22	2.4	0.04	0.01	13.2	0.777	8.44	10.86	0.90					
6904E1	z1	22.42	1.65	11.77	1.8	9.28	2.4	0.79	0.17	19.8	0.842	13.29	15.79	1.03	16.8	1.1	77	10	188
	z2	39.78	1.65	19.56	1.8	10.71	2.4	0.55	0.21	20.0	0.833	14.90	17.89	1.21					
6904P2	z1	15.59	1.66	12.09	1.8	4.10	2.4	0.34	0.07	7.3	0.839	9.89	11.78	0.79	11.4	0.4	81	40	203

Table 3. (continued)

Sample	aliq.	He vol. [ncc]	He 1σ [%]	U238 mass [ng]	U238 1σ [%]	Th232 mass [ng]	Th232 1σ [%]	Th/U ratio	Sm mass [ng]	Sm 1σ [%]	Ejection Correct. (Ft)	Uncorr. He-age [Ma]	Ft-Corr. He-age [Ma]	2σ [Ma]	Sample Unweighted Aver. age [Ma]	±2 s.e. [Ma]	Equiv. sphere Radius [μm]	Cooling Rate [°C/Myr]	Closure Temperature [°C]
	z2	13.39	1.66	9.87	1.8	3.27	2.4	0.33	0.17	6.5	0.845	10.41	12.32	0.81					
	z3	8.36	1.68	6.43	1.8	3.14	2.4	0.49	0.09	6.4	0.850	9.66	11.36	0.73					
	z4	7.19	1.69	6.21	1.8	2.83	2.4	0.46	0.13	11.0	0.848	8.66	10.21	0.67					
6905A1	z1	3.17	1.72	3.05	1.8	1.03	2.4	0.34	0.06	17.1	0.834	7.97	9.56	0.66	9.3	0.4	77	40	202
	z2	4.14	1.71	3.95	1.8	0.91	2.4	0.23	0.03	17.8	0.838	8.23	9.82	0.67					
	z3	4.80	1.70	5.16	1.8	1.27	2.4	0.25	0.05	17.6	0.842	7.27	8.63	0.58					
997B1	z3	3.88	1.74	13.47	1.8	2.01	2.4	0.15	0.02	6.7	0.822	2.31	2.81	0.20	3.0	0.2	74	60	206
	z4	5.81	1.70	17.44	1.8	3.31	2.4	0.19	0.10	4.9	0.841	2.64	3.14	0.21					
998C1	z1	9.05	1.67	19.64	1.8	2.61	2.4	0.13	0.10	18.0	0.863	3.70	4.29	0.27	4.4	0.1	85	60	209
	z2	4.19	1.73	9.06	1.8	2.02	2.4	0.22	0.08	18.3	0.846	3.64	4.30	0.29					
	z3	9.03	1.67	18.05	1.8	2.34	2.4	0.13	0.05	18.5	0.848	4.02	4.74	0.31					
998F1	z1	0.53	2.55	1.29	1.8	0.60	2.4	0.46	0.02	8.0	0.815	3.09	3.79	0.31	3.0	0.9	66	60	203
	z2	0.46	2.79	1.12	1.8	0.25	2.4	0.22	0.01	9.5	0.815	3.27	4.01	0.34					
	z3	0.14	3.99	1.07	1.8	0.33	2.4	0.31	0.01	7.6	0.806	1.04	1.28	0.13					
9911D1	z1	5.82	1.69	6.13	1.8	2.20	2.4	0.36	0.03	19.1	0.807	7.25	8.99	0.67	9.6	0.4	64	50	201
	z2	2.44	1.80	2.06	1.8	1.46	2.4	0.71	0.04	19.5	0.806	8.40	10.43	0.78					
	z3	4.93	1.69	5.08	1.8	1.76	2.4	0.35	0.02	8.8	0.802	7.44	9.27	0.70					
9914B1	z1	12.97	1.66	16.36	1.8	1.11	2.4	0.07	0.01	10.6	0.810	6.47	7.99	0.59	8.2	0.2	65	50	201
	z2	9.90	1.68	11.55	1.8	1.16	2.4	0.10	0.02	8.6	0.816	6.94	8.50	0.62					
	z3	8.14	1.69	10.13	1.8	1.37	2.4	0.14	0.03	6.9	0.805	6.45	8.01	0.60					
9916H1	z1	44.76	1.64	6.63	1.8	1.27	2.4	0.19	0.04	7.1	0.809	53.30	65.86	4.87	56.9	4.8	63	3	173
	z2	17.29	1.65	3.05	1.8	0.91	2.4	0.30	0.03	9.2	0.793	43.77	55.17	4.28					
	z3	25.06	1.65	4.81	1.8	1.48	2.4	0.31	0.04	6.7	0.808	40.12	49.64	3.67					
9917A1	z1	42.03	1.64	7.49	1.8	4.69	2.4	0.63	0.17	5.9	0.819	40.36	49.27	3.48	64.2	5.0	71	3	175
	z2	49.75	1.64	6.57	1.8	2.21	2.4	0.34	0.09	6.0	0.825	57.83	70.09	4.90					
	z3	84.72	1.64	10.51	1.8	5.85	2.4	0.56	0.24	5.6	0.838	58.70	70.08	4.66					
	z4	59.85	1.64	8.06	1.8	4.06	2.4	0.50	0.22	10.8	0.813	54.75	67.38	4.87					
9921A1	z1	11.58	1.68	3.37	1.8	3.10	2.4	0.92	0.10	5.8	0.807	23.31	28.87	2.11	40.7	6.7	72	10	187
	z2	29.96	1.65	4.97	1.8	3.35	2.4	0.67	0.14	5.9	0.825	42.90	52.02	3.60					
	z3	22.41	1.66	4.51	1.8	3.44	2.4	0.76	0.11	6.0	0.842	34.75	41.28	2.70					

[a]Ejection correct. (Ft): correction factor for alpha-ejection (according to *Farley et al.* [1996] and *Hourigan et al.*, [2005]). Uncertainty of the single grain age is given as 2 sigma, and it includes both the analytical uncertainty and the estimated uncertainty of Ft. Uncertainty of average age is 2 standard error, as $(SD)/(n)^{1/2}$; where SD = standard deviation of the age replicates and n = number of age determinations. Closure temperature after *Dodson* [1973], calculated for each sample from cooling rate and equivalent sphere radius, based on diffusion data of *Reiners et al.* [2004].

[b]not included in calculation of average sample age.

Table 4. Apatite Fission Track Data[a]

Sample	Irradiation	Areas	N_s	N_i	χ^2	$P(\chi^2)$	$\zeta \pm 1\sigma$	$\rho_d \pm 1\sigma$ [10^6 cm^{-2}]	Mount Age ± 1σ [Ma][b]	Sample Age ± 1σ [Ma]	Cooling Rate [°C/Myr]	T_c [°C][e]
4726A1	FG10	24	294	2024	45.36	0.66	271.5 ± 2.6	0.369 ± 0.015	7.3 ± 0.5	7.3 ± 0.5	50	130
4726C1	FG20	20	982	2589	131.78	0.00	254.3 ± 4.2	0.560 ± 0.005	27.0 ± 1.1	27.0 ± 1.1	10	116
4726D1	FG10	19	173	400	14.76	1.00	271.5 ± 2.6	0.361 ± 0.015	21.2 ± 2.1	21.2 ± 2.1	10	116
4726G1	FG25	20	1742	5586	30.10	0.00	241.4 ± 8.4	0.239 ± 0.005	9.0 ± 0.4	9.0 ± 0.4	10	116
4726K1	Goe112	80	392	7626	131.03	0.00	389.1 ± 6.8	0.573 ± 0.067	5.7 ± 0.7	5.7 ± 0.7	40	128
4727A1	FG10	29	330	3254	26.75	1.00	271.5 ± 2.6	0.344 ± 0.015	4.7 ± 0.3	4.7 ± 0.3	40	128
4727A2a	Goe112	60	192	4023	54.89	0.63	389.1 ± 6.8	0.580 ± 0.067	5.4 ± 0.7			
4727A2b	FG20	22	67	1095	43.99	0.00	254.3 ± 4.2	0.558 ± 0.005	4.3 ± 0.6	4.8 ± 0.5[c]	40	128
4727C1	FG10	22	286	1670	18.09	0.98	271.5 ± 2.6	0.369 ± 0.015	8.6 ± 0.7	8.6 ± 0.7	40	128
6821A1	FG20	27	236	3242	61.69	0.00	254.3 ± 4.2	0.549 ± 0.005	5.1 ± 0.4	5.1 ± 0.4	60	132
6822C1	FG20	27	90	3218	52.15	0.00	254.3 ± 4.2	0.552 ± 0.005	2.0 ± 0.2	2.0 ± 0.2	60	132
6822D1	FG20	43	205	4777	87.03	0.00	254.3 ± 4.2	0.555 ± 0.005	3.0 ± 0.2	3.0 ± 0.2	60	132
6822E1	FG20	19	133	4510	18.62	0.42	254.3 ± 4.2	0.557 ± 0.005	2.1 ± 0.2	2.1 ± 0.2	60	132
6822T1	FG20	20	145	2532	51.91	0.00	254.3 ± 4.2	0.560 ± 0.005	4.1 ± 0.4	4.1 ± 0.4	20	122
6822W1	FG20	21	221	7092	39.80	0.01	254.3 ± 4.2	0.564 ± 0.005	2.2 ± 0.2	2.2 ± 0.2	20	122
6823A3	FG17	29	129	1736	42.73	0.10	271.3 ± 3.1	0.354 ± 0.005	3.6 ± 0.3	3.6 ± 0.3	60	132
6823C1	FG16	32	177	1459	35.67	1.00	269.6 ± 5.2	0.193 ± 0.004	3.2 ± 0.3	3.2 ± 0.3	50	130
6824B4a	FG16	24	102	366	11.80	1.00	269.6 ± 5.2	0.193 ± 0.004	7.3 ± 0.8			
6824B4b	FG17	35	222	1561	39.17	0.46	271.3 ± 3.1	0.354 ± 0.005	6.8 ± 0.5	6.9 ± 0.4[c]	50	130
6824D1	FG16	33	255	1488	56.51	0.88	269.6 ± 5.2	0.194 ± 0.004	4.5 ± 0.3	4.5 ± 0.3	50	130
6824E1	FG16	37	67	227	34.16	0.69	269.6 ± 5.2	0.195 ± 0.004	7.8 ± 1.1	7.8 ± 1.1	50	130
6824F1	FG16	33	69	290	28.85	1.00	269.6 ± 5.2	0.196 ± 0.004	6.3 ± 0.9	6.3 ± 0.9	50	130
6824F1	FG20	24	110	716	62.89	0.00	254.3 ± 4.2	0.562 ± 0.005	11.0 ± 1.1[d]			
6824H1a	FG16	41	200	1334	30.69	1.00	269.6 ± 5.2	0.196 ± 0.004	4.0 ± 0.3			
6824H1b	FG16	44	143	918	26.04	1.00	269.6 ± 5.2	0.197 ± 0.004	4.1 ± 0.4	4.0 ± 0.2[c]	50	130
6825B1	FG16	28	30	168	17.16	1.00	269.6 ± 5.2	0.198 ± 0.004	4.8 ± 1.0	4.8 ± 1.0	50	130
6826B1	FG17	13	34	268	16.40	1.00	271.3 ± 3.1	0.354 ± 0.005	6.1 ± 1.1	6.1 ± 1.1		
6826D1a	FG17	28	159	1319	43.86	0.27	271.3 ± 3.1	0.354 ± 0.005	5.8 ± 0.5			
6826D1b	FG17	20	127	832	10.33	0.99	271.3 ± 3.1	0.354 ± 0.005	7.3 ± 0.7	6.3 ± 0.4[c]	40	128
6827A1	Goe112	80	559	6765	64.34	0.88	389.1 ± 6.8	0.586 ± 0.067	9.4 ± 1.2	9.4 ± 1.2	40	128
6827A2	FG17	43	544	3273	51.54	0.38	271.3 ± 3.1	0.354 ± 0.005	8.0 ± 0.4			
6827A2	FG16	73	1031	2970	105.54	0.55	269.6 ± 5.2	0.199 ± 0.004	9.3 ± 0.4	8.7 ± 0.3[c]	40	128
6828A1	FG17	5	5	101	1.08	1.00	271.3 ± 3.1	0.354 ± 0.005	2.4 ± 1.1[d]			
6829A1	Goe112	100	432	5123	89.06	0.75	389.1 ± 6.8	0.592 ± 0.067	9.7 ± 1.2	9.7 ± 1.2	40	128
6829B1	FG16	22	79	251	15.47	1.00	269.6 ± 5.2	0.197 ± 0.004	8.4 ± 1.1	8.4 ± 1.1	40	128
6829C1	FG16	47	358	1186	46.96	0.98	269.6 ± 5.2	0.196 ± 0.004	8.0 ± 0.5	8.0 ± 0.5	40	128
6831A1	FG20	17	1027	8002	197.08	0.00	254.3 ± 4.2	0.567 ± 0.005	9.2 ± 0.4	9.2 ± 0.4	40	128
6831C3	FG16	67	581	2398	77.54	0.49	269.6 ± 5.2	0.195 ± 0.004	6.4 ± 0.3	6.4 ± 0.3	40	128
6901A2	Goe112	80	732	8464	109.47	0.01	389.1 ± 6.8	0.599 ± 0.067	10.1 ± 1.2	10.1 ± 1.2	40	128
6901B1a	Goe112	39	389	4735	36.79	0.53	389.1 ± 6.8	0.611 ± 0.067	9.8 ± 1.2			
6901B1b	Goe112	60	708	8131	73.83	0.09	389.1 ± 6.8	0.605 ± 0.067	10.2 ± 1.2	10.0 ± 0.8[c]	40	128
6901C1	FG20	24	269	3217	70.81	0.00	254.3 ± 4.2	0.568 ± 0.005	6.0 ± 0.4	6.0 ± 0.4	40	128
6901D1	FG16	67	964	1580	52.76	0.94	269.6 ± 5.2	0.193 ± 0.004	15.9 ± 0.8	15.9 ± 0.8	10	116
6901E1a	FG16	42	375	558	37.83	1.00	269.6 ± 5.2	0.192 ± 0.004	17.4 ± 1.3			
6901E1b	FG16	82	505	888	68.61	1.00	269.6 ± 5.2	0.191 ± 0.004	14.6 ± 0.9	15.5 ± 0.7[c]	10	116
6902B1	Goe112	111	181	3279	142.62	0.02	389.1 ± 6.8	0.617 ± 0.067	6.6 ± 0.9	6.6 ± 0.9	10	116
6902G1	FG20	20	305	5465	161.60	0.00	254.3 ± 4.2	0.569 ± 0.005	4.0 ± 0.2	4.0 ± 0.2	10	116
6903B1	Goe112	66	445	8121	96.70	0.01	389.1 ± 6.8	0.624 ± 0.067	6.6 ± 0.8	6.6 ± 0.8	10	116
6903C1a	FG16	49	248	1707	74.05	0.02	269.6 ± 5.2	0.190 ± 0.004	3.7 ± 0.3			
6903C1b	FG16	21	80	541	33.65	0.07	269.6 ± 5.2	0.189 ± 0.004	3.8 ± 0.5	3.7 ± 0.3[c]	10	116
6904G1a	FG20	20	381	4277	73.96	0.00	254.3 ± 4.2	0.570 ± 0.005	6.5 ± 0.4			

Table 4. (continued)

Sample	Irradiation	Areas	N_s	N_i	χ^2	$P(\chi^2)$	$\zeta \pm 1\sigma$	$\rho_d \pm 1\sigma$ [10^6 cm^{-2}]	Mount Age ± 1σ [Ma][b]	Sample Age ± 1σ [Ma]	Cooling Rate [°C/Myr]	T_c [°C][e]
6904G1b	FG20	20	444	5179	85.37	0.00	254.3 ± 4.2	0.570 ± 0.005	6.2 ± 0.3	6.3 ± 0.2[c]	10	116
6904M1	FG20	30	289	2250	126.23	0.00	254.3 ± 4.2	0.570 ± 0.005	9.3 ± 0.6	9.3 ± 0.6	40	128
6904M2	FG20	19	74	322	21.10	0.27	254.3 ± 4.2	0.569 ± 0.005	16.6 ± 2.2[d]			
6904P1	FG20	20	399	3067	54.48	0.00	254.3 ± 4.2	0.568 ± 0.005	9.4 ± 0.5	9.4 ± 0.5	40	128
6904Q3	Goe112	80	563	6644	75.89	0.58	389.1 ± 6.8	0.630 ± 0.067	10.4 ± 1.2	10.4 ± 1.2	40	128
6905A1	FG20	20	218	1828	30.20	0.05	254.3 ± 4.2	0.567 ± 0.005	8.6 ± 0.6	8.6 ± 0.6	40	128
6905B1	Goe112	60	256	3232	61.58	0.38	389.1 ± 6.8	0.636 ± 0.067	9.8 ± 1.2	9.8 ± 1.2	40	128
6905B2	FG16	50	529	1690	56.00	1.00	269.6 ± 5.2	0.188 ± 0.004	7.9 ± 0.5			
6905B2	FG16	57	607	1649	47.36	0.98	269.6 ± 5.2	0.186 ± 0.004	9.2 ± 0.5	8.6 ± 0.4[c]	40	128
9911A3	FG54	40	961	5709	54.60	0.10	241.4 ± 8.4	0.228 ± 0.005	4.6 ± 0.2	4.6 ± 0.2	50	130
9912B1	FG54	29	1197	6600	41.30	0.70	241.4 ± 8.4	0.232 ± 0.005	5.1 ± 0.2	5.1 ± 0.2	50	130
9912C1	Goe112	80	587	6882	93.56	0.13	389.1 ± 6.8	0.668 ± 0.067	11.1 ± 1.2	11.1 ± 1.2	50	130
9914D2	FG54	37	682	2801	51.00	3.10	241.4 ± 8.4	0.235 ± 0.005	6.9 ± 0.4	6.9 ± 0.4	50	130
9914D4	Goe112	139	192	2250	151.13	0.23	389.1 ± 6.8	0.685 ± 0.067	11.4 ± 1.4	11.4 ± 1.4	50	130
9915A2	Goe112	60	139	1799	74.80	0.08	389.1 ± 6.8	0.690 ± 0.067	10.4 ± 1.4	10.4 ± 1.4	50	130
9916H1	Goe112	65	464	1621	110.79	0.00	389.1 ± 6.8	0.695 ± 0.067	38.6 ± 4.3	38.6 ± 4.3	3	107
9917B1	Goe112	80	204	1584	88.59	0.22	389.1 ± 6.8	0.706 ± 0.067	17.7 ± 2.2	17.7 ± 2.2	3	107
9918B1	FG54	21	572	2234	31.40	0.00	241.4 ± 8.4	0.240 ± 0.005	7.4 ± 0.4	7.4 ± 0.4	50	130
996A1	Goe112	62	216	4075	56.11	0.65	389.1 ± 6.8	0.643 ± 0.067	6.6 ± 0.8	6.6 ± 0.8	20	122
997B1	Goe112	100	181	8467	91.51	0.69	389.1 ± 6.8	0.649 ± 0.067	2.7 ± 0.3	2.7 ± 0.3	60	132
998C1	Goe112	80	143	3768	104.17	0.03	389.1 ± 6.8	0.655 ± 0.067	4.8 ± 0.6	4.8 ± 0.6	60	132
999B5	Goe112	71	122	5596	91.70	0.04	389.1 ± 6.8	0.662 ± 0.067	2.8 ± 0.4	2.8 ± 0.4	60	132
P2s[f]		62[f]	57[f]	504[f]		0.99[f]	401.2 ± 9.9[e]	0.471[f]		10.7 ± 1.5[f]	20	122
P5s[f]		49[f]	57[f]	789[f]		0.04[f]	401.2 ± 9.9[e]	0.526[f]		10.1 ± 1.7[f]	20	122

[a] N_s, N_i: number of spontaneous, induced tracks; ρ_d: induced track density from glas standard, extrapolated to the respective position of the mount within the irradiation batch.
[b] pooled ζ-ages.
[c] weighted average.
[d] rejected.
[e] closure temperature [*Dodson*, 1973], calculated based on annealing kinetics of *Ketcham et al*. [1999].
[f] data from *Schwab* [2004].

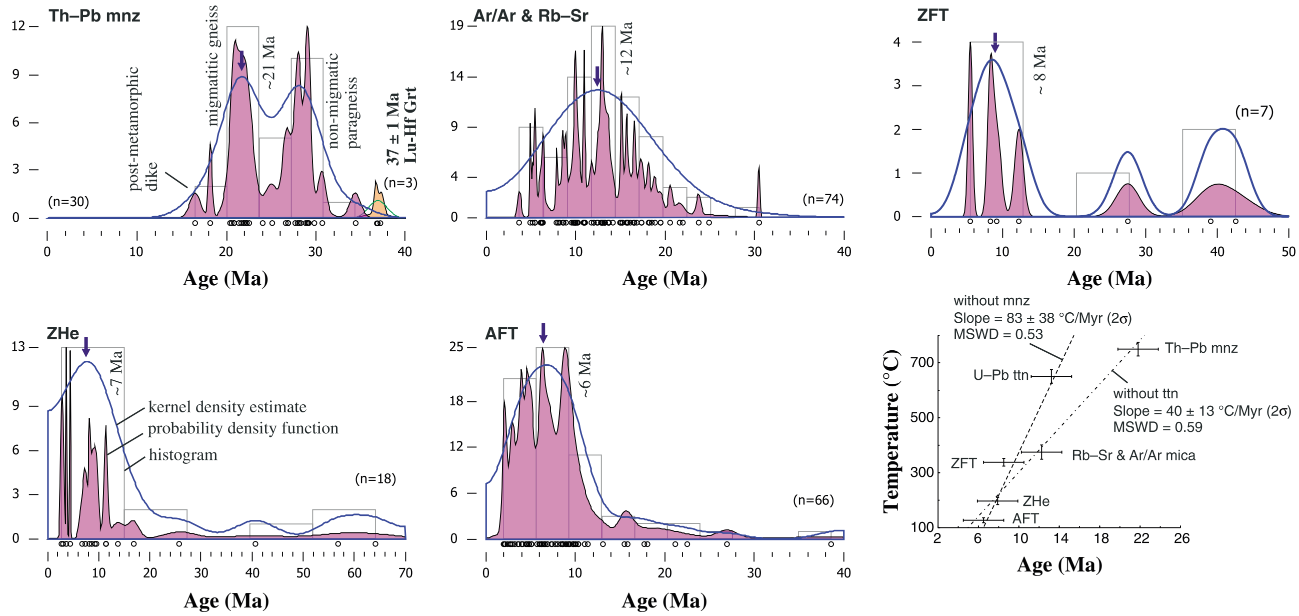

Figure 3. Summary of new and published geo-thermochronologic data from the southern Pamir, displayed in histograms, probability density functions, and kernel-density estimate curves (see *Vermeesch* [2012] for definitions and implementation). Bottom-right diagram shows bulk cooling paths calculated from the age peaks marked in the data plots and mean closure temperatures obtained from sample estimates (Tables 1–4).

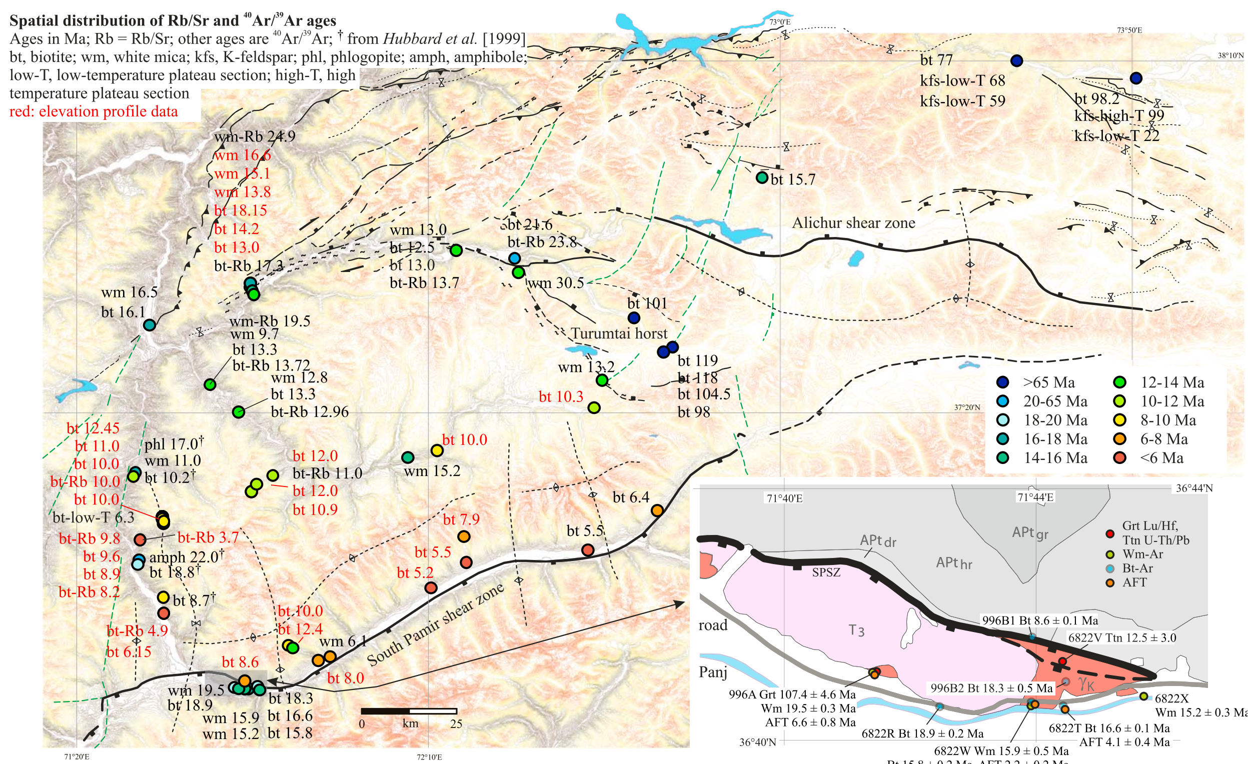

Figure 4. Rb-Sr and $^{40}Ar/^{39}Ar$ ages (see Tables 1 and S4, and *Hubbard et al.* [1999]) on a simplified structural and topographic map of the southern Pamir. Symbol colors indicate age. Data used in age-elevation plots of Figure 8 are in red. Inset documents age offset across South Pamir shear zone. Lithological units after *Vlasov et al.* [1991]: APt_{gr} and APt_{hr}, gneiss; T_3, Triassic slates; γ_k, Cretaceous granitoid. Additional abbreviations are Grt, garnet Lu-Hf; Ttn, titanite U-Pb; AFT, apatite fission track.

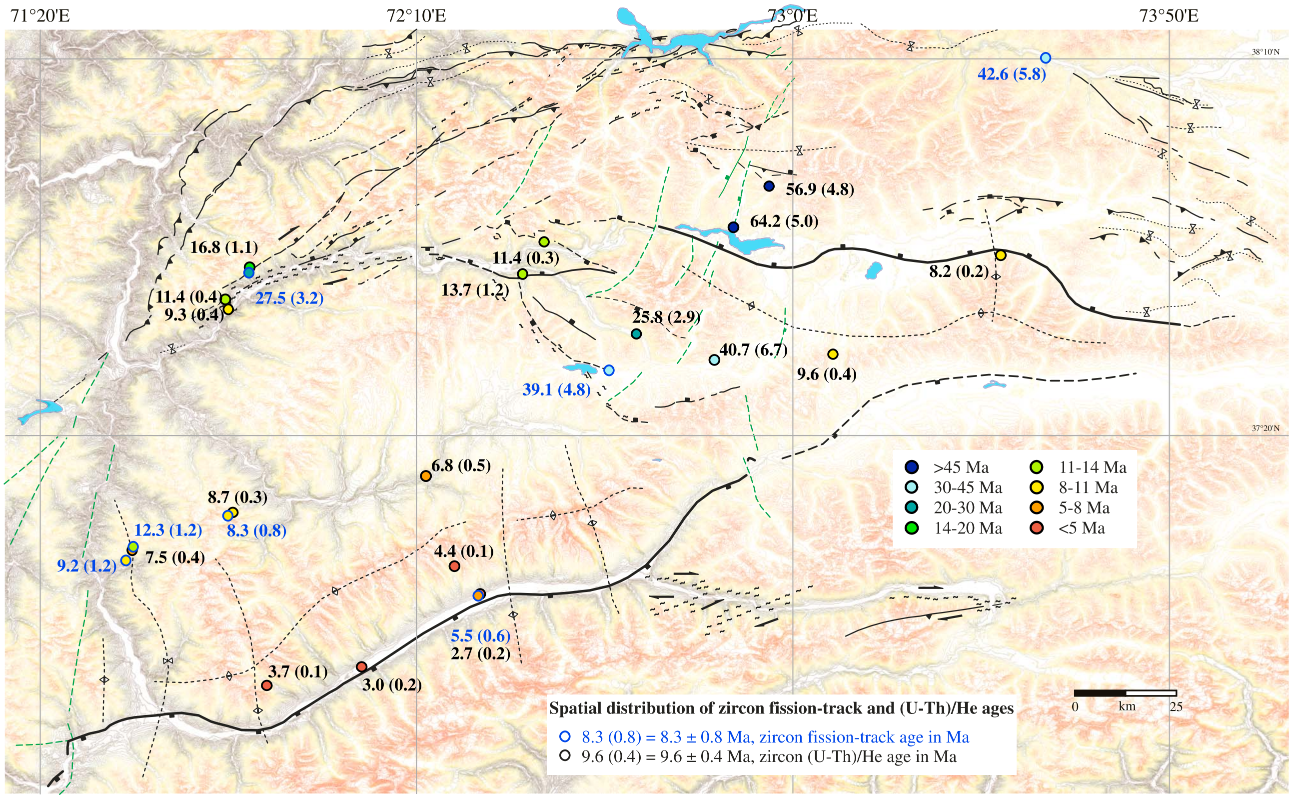

Figure 5. Zircon fission track (blue) and zircon (U-Th)/He ages (black). Errors (ZFT, 1σ; ZHe, 2σ) are given in parentheses (see Tables 2 and 3).

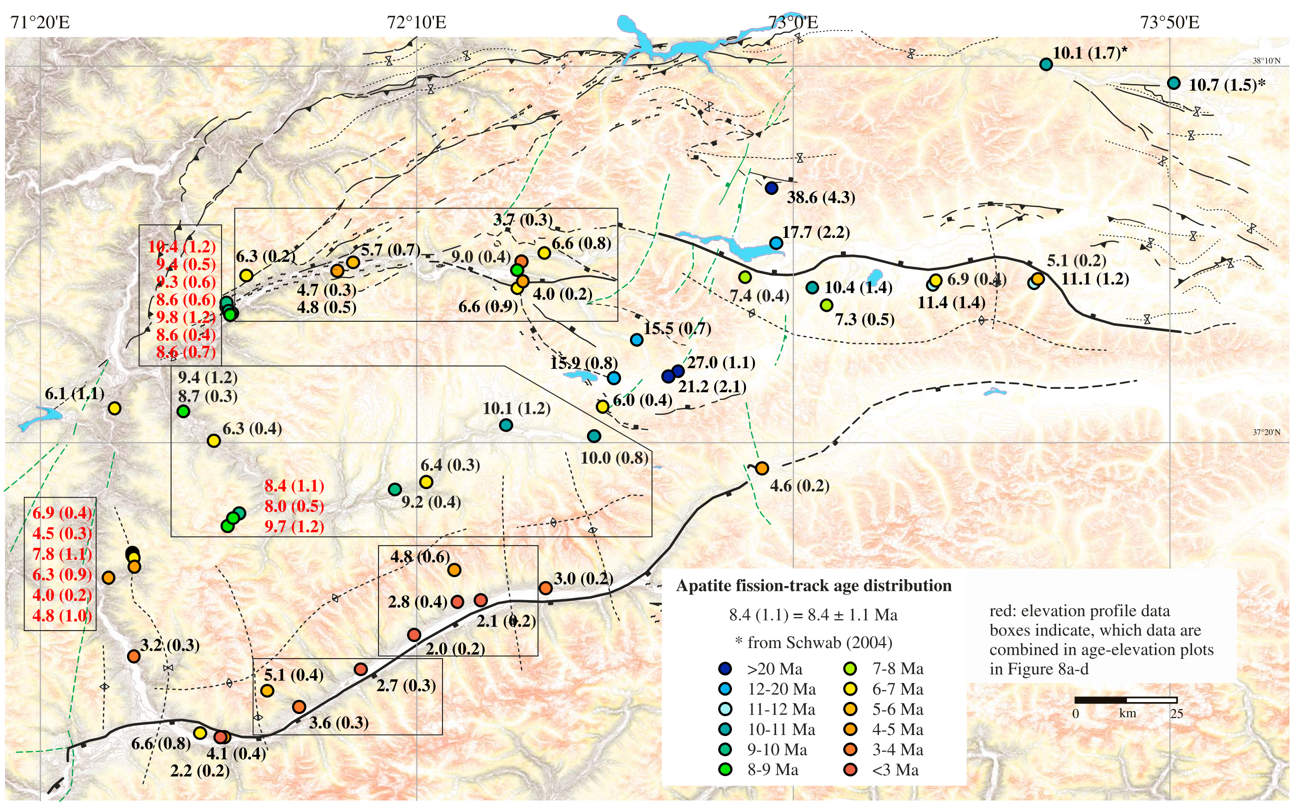

Figure 6. Apatite fission track ages with 1σ errors in parentheses (Table 4). Two ages from the southeastern Pamir are from *Schwab* [2004]. "Elevation profiles," i.e., samples that span a range of altitudes with little variation in latitude and longitude are red; ages that are combined in the age-elevation plots of Figure 8 are marked by boxes.

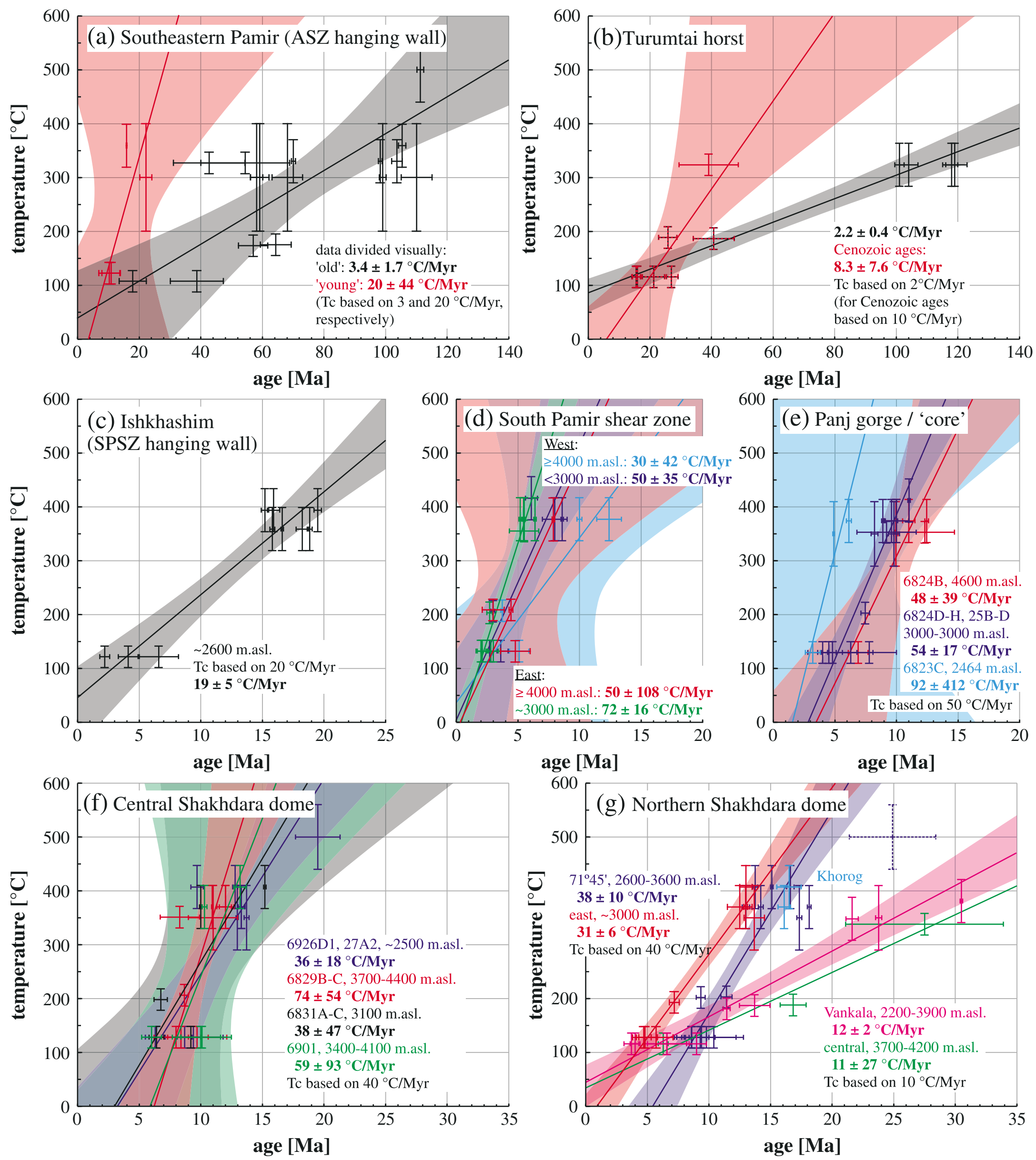

Figure 7. Cooling trends from multiple-thermochronometer data from (a) the southeastern Pamir; (b) the low-strain Turumtai horst between the Alichur and Shakhdara domes; (c) the South Pamir shear zone (SPSZ) hanging wall (see Figure 2); (d) the western (gray, blue) and eastern (red, green) SPSZ; (e) the core of the dome along the Panj gorge; (f) the central Shakhdara dome, and (g) the northern Shakhdara dome. Where samples of different localities are shown in one plot, sample numbers and elevations are given. In Figure 7g, sample localities are from west to east: "Khorog," "east," "71°45′E," "central," and "Vankala." Cooling trends were determined by linear regression using age as dependent variable; data points were weighted equally (ISOPLOT [*Ludwig*, 2008]). Error bars are 2σ, error envelopes are 95% confidence. In Figures 7a and 7b, two trends have been detected, a slow long-term (Cretaceous-Tertiary) and a Miocene trend of increased cooling rates. Closure temperatures are given in Tables 1–4 and discussed in the text and Appendices A2–A4.

(3.7–2.7 Ma). AFT ages from crystalline rocks within the domes span 11.4 to 2.0 Ma (Figure 6); here, the younging trend is less pronounced.

[16] Where more than one dating method was applied at the same locality, the age order is Wm Rb-Sr > Wm $^{40}Ar/^{39}Ar$ > Bt $^{40}Ar/^{39}Ar$ ≥ Bt Rb-Sr ≥ ZFT > ZHe > AFT, in accordance with inferred closure temperatures. Potential outliers were identified by comparison with other thermochronometers and by regional trends. In particular, one sample from the central Shakhdara dome (6825B1) yielded Bt Rb-Sr (3.7 ± 0.2 Ma) and $^{40}Ar/^{39}Ar$ (15.0 ± 0.5 Ma) ages that are too young and too old, respectively. The AFT age 6828A1 (2.4 ± 1.1 Ma) is significantly younger than several nearby samples. The following analysis does not consider these outliers. For samples 6824B1 and 6824D1, we report two Bt $^{40}Ar/^{39}Ar$ dates based on the step-heating profiles, a low-

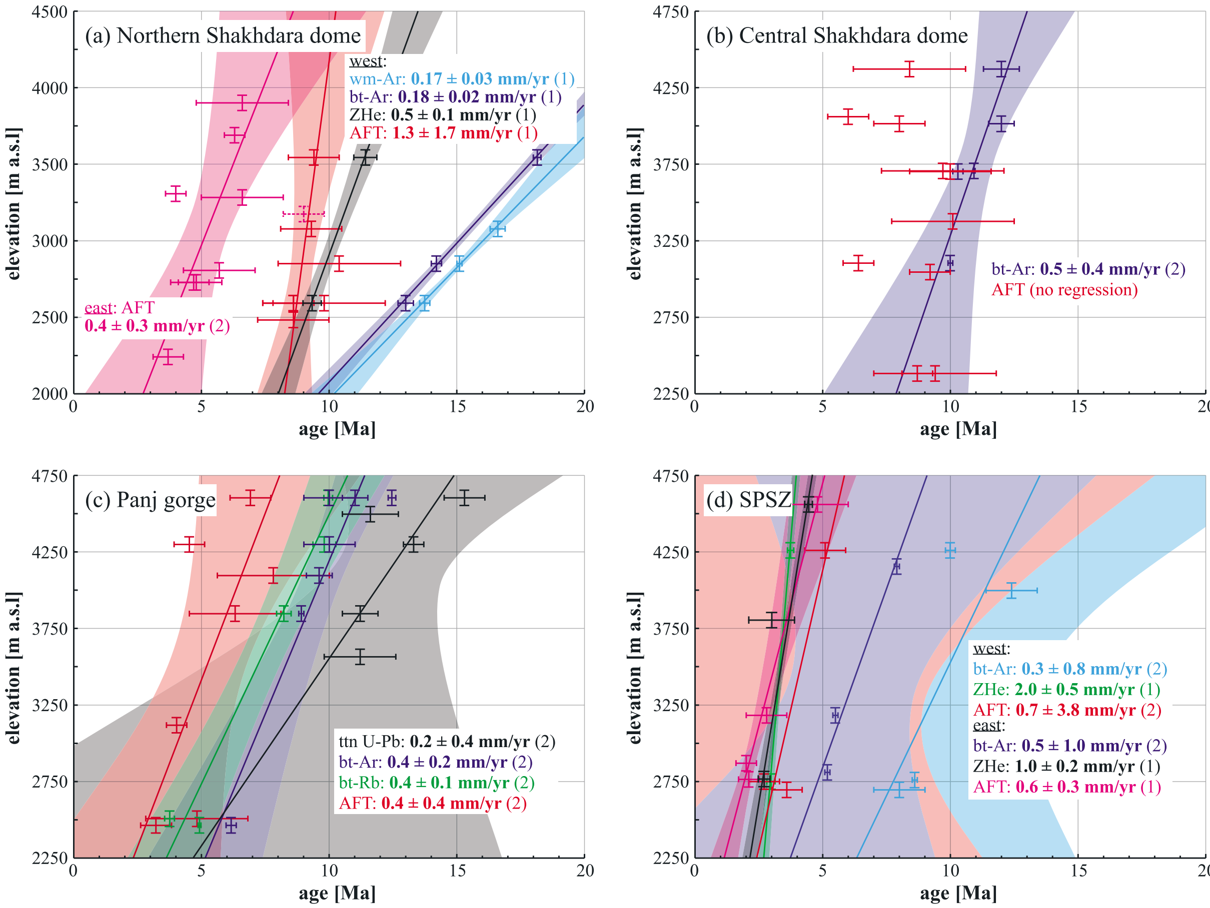

Figure 8. Age-elevation trends from the data marked in red in Figure 4 and by boxes in Figure 6 and selected zircon (U-Th)/He and titanite U-Pb data (Table S2). (a) Northern Shakhdara dome; (b) central Shakhdara dome; (c) Panj gorge/core of the dome; (d) South Pamir shear zone. Error bars are 2σ. Linear regression lines were fitted (ISOPLOT [*Ludwig*, 2008]) using age as dependent variable; (1) is model 1 fit (error weighted), (2) is model 2 fit (unweighted); error envelopes are 2σ and 95%, respectively.

temperature and a high-temperature age. For 6824B1, both ages were included in the cooling paths, elevation, and distance trends; for 6824D1, the low-temperature age (6.3 ± 0.5 Ma) is significantly younger than closeby samples, and only the high-temperature age (10 ± 1 Ma) is evaluated.

[17] Within the Shakhdara dome, the average cooling rates (Figures 7d–g) range from ~30 to 90°C/Myr. The slowest cooling rates were recorded in the eastern GSZ near the Turumtai horst and at high elevations in the western GSZ (Figure 7 g: "Vankala" and "central," ~10°C/Myr; Figure 2 for location names). Two low-elevation localities from the western GSZ yielded 30–40°C/Myr, at the lower end of the rates in the central (35–90°C/Myr, Figures 7e and 7f) and southern parts of the dome (30–70°C/Myr, Figure 7d). In the core of the dome, low-elevation sample 6823C1 yielded a higher cooling rate than high-elevation samples (6824; Figure 7e). Because our data set is dominated by AFT and $^{40}Ar/^{39}Ar$ ages, the cooling rates at most localities are based on these thermochronometers; where ZHe data are available, they suggest that cooling rates are constant or increase with time (Figures 7d and 7f); gradually increasing cooling rates are also supported by two white mica Rb-Sr ages (Figures 7f and 7g).

[18] The least variable age-elevation relationships were obtained in the core of the Shakhdara dome and in the eastern part of the SPSZ (Figures 8c and 8d): titanite U-Pb, Bt Rb-Sr, and Bt $^{40}Ar/^{39}Ar$ age-elevation trends span 0.2–1.0 mm/yr (ZHe in the western SPSZ: 2.0 mm/yr) at both locations. The data from the western part of the SPSZ are less well correlated but consistent with the eastern SPSZ (Figure 8d). In the central Shakhdara dome, the Bt $^{40}Ar/^{39}Ar$ trend of 0.5 mm/yr (Figure 8b) is defined by three samples from an elevation profile and two samples from farther east (see Figure 4). The AFT age-elevation trends in the central and southern parts of the dome are similar to or steeper than those from higher-temperature thermochronometers (0.4 to ≥0.7 mm/yr; Figures 8b–d). Along the northern rim of the Shakhdara dome, Bt and Wm $^{40}Ar/^{39}Ar$ data from the lower, western Gunt valley consistently yield 0.2 mm/yr (Figure 8a, "west"); the ZHe elevation trend from the same locality is steeper (0.5 mm/yr) and close to the AFT trend (1.3 ± 1.7 mm/yr). AFT ages in the upper, eastern Gunt valley (Figure 8a; "east") are younger than samples from the west but define a similar 0.4 ± 0.3 mm/yr age-elevation trend.

[19] We analyzed the hanging wall of the SPSZ at the only exposure on the Tajikistan side of the Panj (Figures 2 and 4

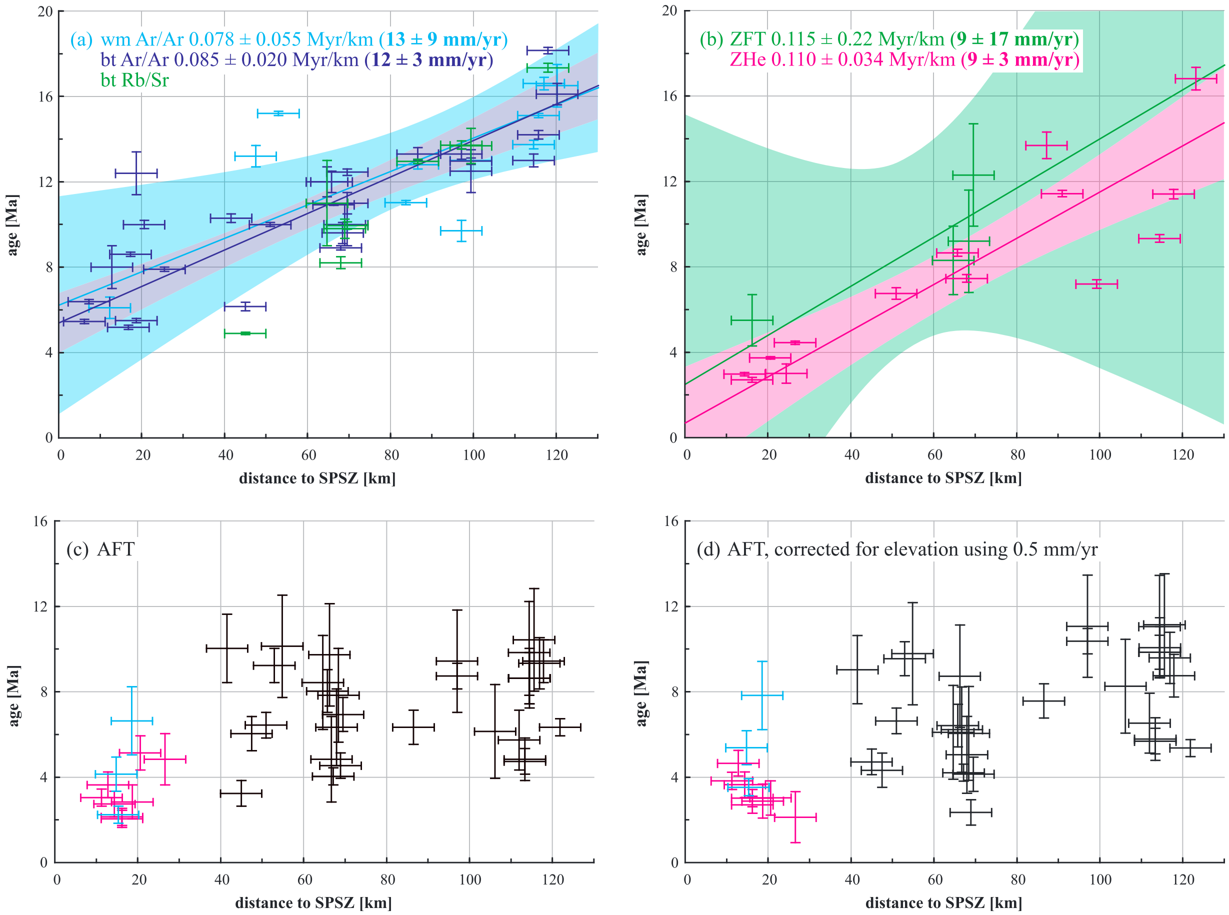

Figure 9. Cooling ages *vs*. distance to the South Pamir shear zone (SPSZ) for (a) Wm and Bt $^{40}Ar/^{39}Ar$ and Rb-Sr ages; (b) zircon fission track and (U-Th)/He ages; (c) apatite fission track ages; (d) elevation-corrected apatite fission track ages: Ages were extrapolated from sample elevation to 3200 m a.s.l. using 0.5 mm/yr (see text for details). Distance to SPSZ is measured parallel to the average stretching lineation (170°). Linear regression is based on age as dependent variable (model 2 fit, ISOPLOT [*Ludwig*, 2008]); slopes are given as age gradient and as apparent slip rate (see text for discussion). In Figures 9c and 9d, pink color indicates the young age cluster near the SPSZ; blue color indicates hanging-wall samples (see text).

inset). Bt $^{40}Ar/^{39}Ar$ ages span 18.9 to 15.8 Ma, Wm ages 19.5 to 15.2 Ma; Wm and Bt ages from the same sample (6822 W1) are identical within error. Our $^{40}Ar/^{39}Ar$ ages record an offset of ~10 Myr across the SPSZ: sample 996B1 from the footwall yielded 8.6 ± 0.1 Ma (Bt), comparable to 8.0 ± 1.0 Ma (Bt, 6823A3) and 6.1 ± 0.5 Ma (Wm, 6822A3) ages obtained 20 km farther east, and younger than two high-elevation Bt $^{40}Ar/^{39}Ar$ ages from the footwall (10.0 ± 0.2 and 12.4 ± 1.0 Ma). In contrast, the AFT ages do not show a significant offset across the SPSZ (Figures 3 and 4 inset): three hanging-wall samples yielded 6.6 ± 0.8 to 2.2 ± 0.2 Ma, footwall samples along the SPSZ span 5.1 ± 0.4 to 2.0 ± 0.2 Ma. The SPSZ hanging wall (Figure 7c) cooled at ~20°C/Myr since at least 19 Ma.

[20] Figure 9 shows cooling ages from the Shakhdara dome as a function of distance to the SPSZ, measured parallel to the average stretching lineation (170°). Because the trace of the SPSZ is curved, we measured the distance to a line parallel to the average SPSZ trend and assigned an error of ±5 km to the distance. Rb-Sr, $^{40}Ar/^{39}Ar$, ZFT, and ZHe show younging trends towards the SPSZ (Figures 9a and 9b). Bt $^{40}Ar/^{39}Ar$ and ZHe data define gradient of 0.085 Myr/km (equivalent to 12 mm/yr) and 0.110 Myr/km (equivalent to 9 mm/yr), respectively; gradients defined by the other thermochronometers have higher uncertainty but are consistent with the ZHe and Bt $^{40}Ar/^{39}Ar$ values. In contrast, we observed no significant N-S age relationship in the AFT data (Figure 9c). Figure 9d shows the N-S gradient for AFT data corrected to a common elevation of 3200 m using the age-elevation gradient of 0.5 mm/yr documented throughout the Shakhdara dome. This analysis shows that the large scatter is not an effect of topography, and that—unlike the higher-temperature thermochronometers—the AFT ages do not vary systematically with distance to the SPSZ, although the youngest AFT ages cluster near the SPSZ (red in Figures 9c and 9d; the blue ages are from the SPSZ hanging wall). A similar elevation correction applied to the Rb-Sr, $^{40}Ar/^{39}Ar$, ZFT, and ZHe data slightly reduces scatter in the data but does not change the observed N-S gradients of ~10 mm/yr. Along the SPSZ, footwall $^{40}Ar/^{39}Ar$ and AFT samples at similar elevations define an along-strike age trend: ages are oldest in the western, youngest in the center, and older again in the eastern stretch of the SPSZ ($^{40}Ar/^{39}Ar$: 8.6–8.0–6.1–5.2–5.5–6.4 Ma; AFT: 3.6–2.7–2.0–2.1–3.0–4.6 Ma).

[21] The Alichur dome is poorly dated, and we have not obtained age-elevation trends or cooling rates yet. Two ZHe ages from the Alichur dome are middle Miocene, similar to the Shakhdara dome; the ZHe age from the dome-bounding ASZ (9914B1: 8.2 ± 0.2 Ma) is younger than 9911D1 (9.6 ± 0.6 Ma; Figure 5) from the interior of the dome, suggesting that in the Alichur dome, too, cooling ages vary with distance to the dome-bounding shear zone. AFT ages from the Alichur dome below the ASZ (11.4 to 5.1 Ma) are younger than two ages from the hanging wall (17.7 ± 2.2, 38.6 ± 4.3 Ma; Figure 6).

[22] In the Turumtai horst, cooling ages are older than in the domes: Bt $^{40}Ar/^{39}Ar$ ages cluster in the mid-Cretaceous (98 ± 4 to 119 ± 4 Ma). One ZFT age (39.1 ± 4.8 Ma), two ZHe ages (40.7 ± 6.7 and 25.8 ± 2.9 Ma), and four AFT ages (15.5–27.0 Ma) indicate slow cooling at ~2°C/Myr through the Late Cretaceous and early Paleogene, followed by more rapid Eocene-Miocene cooling (~10°C/Myr; Figure 7b). Ages from the southeastern Pamir plateau are more variable but consistent with the cooling history determined in the horst: long-term cooling at ~3°C/Myr, followed by faster Cenozoic cooling (Figure 7a). Samples 6902C1–G1, 6903B1–C1 and 4726G1 from the upper Gunt valley (Figure 7 g, Vankala) are located at the transition between the horst and the northeastern margin of the Shakhdara dome; their cooling history is intermediate between those of the dome and the Turumtai horst, with continuous cooling from ≥400°C to ambient temperatures at ~10°C/Myr. AFT ages within the horst (27.0 to 15.5 Ma) are older than adjacent samples from the Alichur and Shakhdara dome crystalline rocks (≤10.1 Ma; Figure 6).

5. Discussion

5.1. Gneiss Domes Within Slowly Exhuming Southern Pamir Crust

[23] High-grade metamorphic rocks, shown as Archean-Proterozoic crystalline rocks in Soviet geologic maps [*Vlasov et al*., 1991], constitute ~30% of the surface exposure of the Pamir. Structural investigations have revealed that the largest of these domes, the southwestern Pamir Shakhdara-Alichur composite dome, was exhumed during ~N-S extension along two low-angle detachments, the SPSZ and the ASZ [*Stübner et al*., 2013] (Figure 2). Titanite, monazite, and zircon U/Th-Pb ages of 30–10 Ma [*Schmidt et al*., 2011] and $^{40}Ar/^{39}Ar$ ages of 18–9 Ma from the core of the dome along the Panj-river gorge [*Hubbard et al*., 1999] suggest Cenozoic metamorphism and exhumation. Our new U-Pb titanite, Rb-Sr, $^{40}Ar/^{39}Ar$ mica, ZFT, and ZHe cooling ages define a Neogene exhumation history and strongly support a *tectonic* exhumation scenario: cooling ages in the footwall (20–2 Ma) are younger than those from the hanging walls of the SPSZ and ASZ and from the Turumtai horst (≥15 Ma); age offsets of 10 Myr (Bt $^{40}Ar/^{39}Ar$) and >30 Myr (ZHe) occur across the SPSZ and ASZ, respectively; and rapid cooling in the Shakhdara dome (35–90°C/Myr) contrasts with slow cooling of the southeastern Pamir plateau and the Turumtai horst (2–10°C/Myr).

[24] Cooling ages from the Turumtai horst and the southeastern Pamir record low cooling rates of ~2–3°C/Myr from the Cretaceous through the early Cenozoic (Figures 7a and 7b), corresponding to long-term erosion rates of ~0.1 mm/yr, independent of upper crustal thermal gradient. We attribute the large scatter in ages from the southeastern Pamir, with ZFT ages as young as 20 Ma, to Cenozoic folding/thrusting and strike-slip shear (Figure 1; *Strecker et al*. [1995]; our unpublished observations). AFT ages from the southeastern Pamir (~39–10 Ma) and the Turumtai horst (27.0–15.5 Ma) suggest that cooling rates increased to ~10–20°C/Myr in the Miocene (Figures 7a and 7b); these may reflect increased exhumation combined with an elevated geothermal gradient as a result of Miocene dome formation. The more rapid cooling in the Miocene means that the conversion of cooling rates to exhumation rates is more sensitive to the assumed thermal gradient: a gradient of 25°C/km yields 0.4–0.8 mm/yr, whereas hotter gradients of 30–45°C/km—more reasonable for the southern Pamir extensional setting—suggest that exhumation rates in the southeastern Pamir and the Turumtai horst may have been on the order of 0.2–0.4 mm/yr. Thus, the accelerated Miocene cooling rates in the horst and southeastern Pamir reflect an increase in both geothermal gradient and in exhumation rate.

5.2. Eocene-Oligocene Crustal Thickening, Migmatization, and the Onset of Extensional Doming

[25] Throughout the Shakhdara-dome crystalline rocks, garnet from amphibolite, pegmatite, and sillimanite gneiss yielded Lu-Hf dates of ~37 Ma (Figure 3); *Smit et al*. [2012] ascribed these dates to prograde metamorphism caused by crustal thickening that predated the formation of the extensional gneiss domes. Monazite Th-Pb dates [*Schmidt et al*., 2011] (Figure 3) from the Shakhdara crystalline rocks range from 34 to 17 Ma and are interpreted to reflect local variability in conditions that favored monazite (re)crystallization. A cluster of monazite dates at ~21 Ma from migmatitic gneisses (Figure 3) likely reflects regrowth of monazite following dissolution into a melt [*Kelsey et al*., 2008]; if this melt freezing occurred during early exhumation, the onset of doming was at ~21 Ma. Alternatively, the age cluster may reflect a pulse of hydrothermal fluid circulation at this time [e.g., *Seydoux-Guillaume et al*., 2002]. We suggest that high-grade metamorphism coupled with regional migmatization weakened the crust sufficiently to facilitate early Miocene gravitational collapse [cf. *Stübner et al*., 2013], possibly inducing further melting by decompression.

[26] The onset of tectonic exhumation of the Shakhdara dome is also reflected in titanite U-Pb dates. One date from a small deformed pegmatite body at the northern rim of the Shakhdara dome (4727A2) and one restite embedded in leucosome from the very top of the SPSZ (997B2) are ~21 Ma (Figure S1); we interpret both as the age of melt extraction during anatexis. The oldest Rb-Sr and $^{40}Ar/^{39}Ar$ ages occur in the Turumtai horst, along the western GSZ of the northern margin of the Shakhdara dome, and in the hanging wall of the SPSZ (Figure 4). The horst preserves Cretaceous ages that record postintrusive cooling (Cretaceous magmatic belt, *Schwab et al*. [2004]); reset ages span 31–13 Ma. The western GSZ ages span 25–13 Ma (mostly ~16 Ma), and those of the hanging wall of the SPSZ 20–15 Ma (mostly ~17 Ma). The rocks of these areas show low-grade metamorphism (except in the near field of Cenozoic dikes and sills) and low-temperature quartz plasticity (300–450°C) during deformation [*Stübner et al*., 2013]. These ages likely record resetting of pre-Cenozoic rocks by regional metamorphism and subsequent cooling through closure induced by crustal extension during

doming. In this interpretation, the ~31 Ma Wm $^{40}Ar/^{39}Ar$ age in the horst dates slow cooling through upper crustal temperatures following Cretaceous magmatism; the ~25 Ma Wm Rb-Sr age in the western GSZ, where Cenozoic metamorphism was higher than in the horst, likely is a formation age acquired during prograde metamorphism. The remaining samples (mostly 20–16 Ma) date cooling from mica formation at 300–500°C through isotopic closure at 350–425°C; this likely occurred during the early stages of upper crustal extension.

5.3. End of Doming and Erosion

[27] The end of doming is indicated by the youngest cooling ages recorded along the southernmost trace of the SPSZ: for $^{40}Ar/^{39}Ar$, these are 5.5–5.2 Ma (Bt) and 6.1 ± 0.5 Ma (Wm); one ZFT age is 5.5 ± 0.6 Ma; and ZHe yielded 2.7–3.0 Ma. The ~10 Myr offset in the Bt $^{40}Ar/^{39}Ar$ ages across the SPSZ implies that cooling through ~400°C resulted from slip along the SPSZ. The AFT ages do not show a significant offset across the SPSZ (blue age symbols in Figures 9c and 9d mark the hanging-wall samples); thus, they suggest that cooling below the AFT closure was dominated by erosional exhumation (but see discussion below).

[28] The reconstruction of the top of the SPSZ based on the distinct lithologic layering of the dome and the local exposure of the top of the shear zone at high elevations (Figure 2b; see also cross sections in *Stübner et al*. [2013]) indicates that up to 2 km, and locally up to 4 km of footwall rocks have been removed from the Shakhdara dome by erosion. We suggest that after several Myr of doming and crustal extension, the lithospheric strength was sufficiently reduced to allow isostatic rebound of the SPSZ footwall, resulting in the gentle fold that defines the dome axis (Figure 2). This isostatic uplift accounts for the erosion observed in the southern Shakhdara dome. The north-flowing part of the Panj, the Panj gorge, deeply incises the core of the dome, creating 2–3 km local relief (Figure 2c in *Stübner et al*. [2013]). The reconstruction of the SPSZ indicates >2 km of erosion in the Panj gorge. The AFT age-elevation profiles in the dome core, close to the major rivers of the area (Panj, Shakhdara; Figures 8b and 8c), support rapid exhumation that we interpret to record mostly fluvial incision. In contrast to the dome interior, the southernmost SPSZ and its hanging wall (i.e., the upper Panj valley) show little signs of erosion: along this valley, the top of the SPSZ is exposed over a distance ≥150 km; evenly spaced wineglass-shaped canyons that result from incision since the last deglaciation. The preservation of Cenozoic pre- to syn-orogenic sedimentary strata along the western SPSZ (in the southwestward continuation of the upper Panj valley in Afghanistan; *Stübner et al*. [2013]) further suggests that the southernmost part of the Shakhdara dome has undergone minimal erosion. If cooling through ZHe and AFT closure in the southernmost Shakhdara crystalline rocks was not governed by erosion, but occurred predominantly by tectonic exhumation, the youngest ages (ZHe, 3.0–2.7 Ma; AFT, 3.6–2.0 Ma, Figures 5 and 6) approximate the end of doming; thus, the ~N-S extension terminated at ~2 Ma. This conclusion is consistent with the absence of fault scarps cutting river terraces and glacial deposits in the upper Panj valley. In addition, active seismicity in the Shakhdara dome and the Wakhan lacks indications for ~N-S extension, but implies a radically different deformation field, i.e., ~E-W extension; the latter is compatible with regional graben formation and sinistral transtensional faulting across much of the Pamir (e.g., Karakul rift; Figure 1; *Sippl et al*. [2013]; *Stübner et al*. [2013]).

[29] If our inference of minimal erosion is correct, the cluster of young AFT ages near the SPSZ (Figures 9c and 9d, blue symbols) reflects the last increment of tectonic exhumation. Thus, why is there no or little offset of the AFT ages across the SPSZ, as recorded in the footwall and the hanging-wall sliver in the southwestern Pamir? The young AFT ages in this SPSZ hanging-wall sliver (6.6–2.2 Ma; Figures 4 inset, 6, and 7c) could be the result of locally enhanced erosion that affected the core of the dome and its southwards continuation along the Panj gorge (Figure 2). Extending this argument, the AFT age-elevation trends in the northern and central dome and in the Panj gorge (Figures 8a–c) may record incision of the Gunt, Shakhdara, and Panj rivers, respectively. Rapid footwall exhumation along a low-angle detachment implies that rivers incised the crystalline basement after the footwall rocks completed tectonic exhumation (as opposed to the hanging wall of thrusts, where erosion coexists with thickening). Therefore, thermal relaxation—not heat advection—likely affected the AFT age-elevation trends. Furthermore, the short wavelength of the topographic relief minimizes the effect of topography on AFT age-elevation trends [e.g., *Ehlers*, 2005]. Both topography and thermal relaxation, however, result in an overestimation of erosion rate by elevation trends, and, thus, we interpret the rates 0.4 to 1.3 mm/yr (Figures 8a–c) as the upper limit for incision of the Panj gorge, and the Shakhdara and Gunt rivers; note that the elevation profile in the central Shakhdara dome, encompassing 2000 m of elevation (Figure 8b), yielded indistinguishable AFT ages. We propose that river incision occurred at up to ~1 mm/yr; erosion rates outside the major river sections are probably lower and ~0.5 mm/yr. The AFT age-elevation trends along the SPSZ (0.6–0.7 mm/yr; Figure 8d) are similar to those throughout the dome; in our interpretation, and because of the dearth of erosion along most of the SPSZ (see above), they result—at least in part—from tectonic exhumation.

[30] Cooling ages vary along the strike of the SPSZ (see above) with the youngest Bt $^{40}Ar/^{39}Ar$ and AFT ages recorded at ~72°10′ E (Figures 4 and 6). The concordance in age trends suggests that high- and low-temperature cooling in the southern Shakhdara are genetically linked. The young ages near 72°10′ E reflect most rapid exhumation in the central part of the SPSZ, probably coupled with a thermal high in this area. This is, however, not necessarily evidence for cooling below AFT closure by tectonic exhumation: lateral variations in the thermal gradient would have outlasted doming and produced a similar pattern in AFT ages, if post-tectonic erosion was sufficiently rapid.

[31] In conclusion, we propose that doming ended at ~2 Ma and that the 30–40 km of exhumation was overwhelmingly tectonic and caused by normal shear on the SPSZ low-angle detachment zone. The amount of erosion along the upper, SW-flowing Panj was minimal. Within the Shakhdara dome, where large areas are drained by the deeply incising ~N-flowing Panj and Shakhdara river systems, the incision rates along these rivers were ~1.0 mm/yr. Erosion outside these drainages was slower (~0.5 mm/yr) and regionally variable with larger amounts in the southern (along the dome axis) than in the northern Shakhdara dome. We suggest that

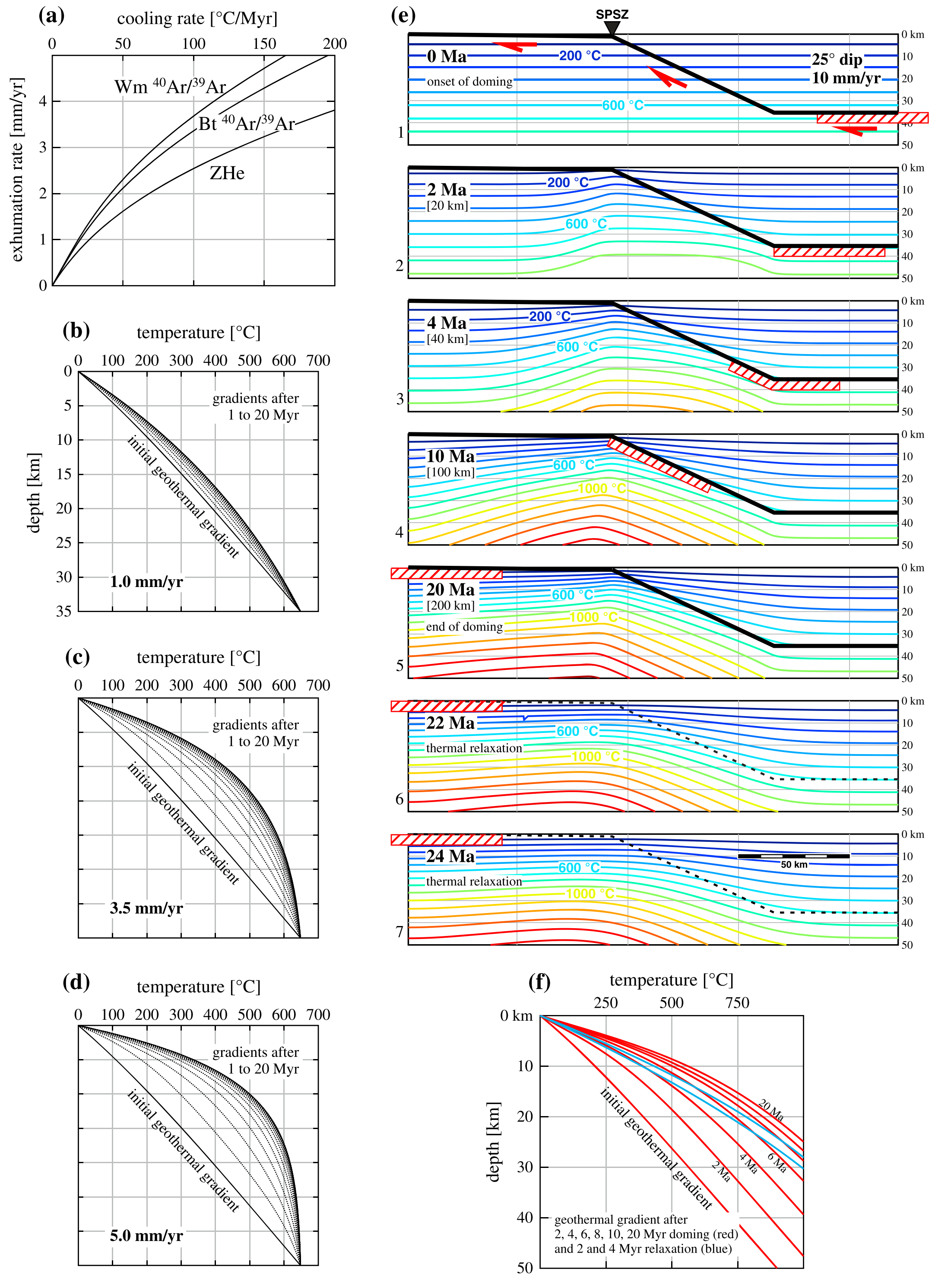

Figure 10. (a) Exhumation rate as a function of cooling rate for white mica (Wm), biotite (Bt) $^{40}Ar/^{39}Ar$, and zircon (U-Th)/He (ZHe), calculated with the program Age2Edot [*Brandon et al.*, 1998]. Model parameters were: depth to layer of constant temperature, 35 km; thermal diffusivity, 34.7 km^2/Myr; internal heat production, 8°C/Myr; surface temperature, 0°C; surface thermal gradient at no erosion, 22°C/km. (b–d) Geothermal gradients resulting from a given initial gradient of ~22°C/km after 1 to 20 Myr (1 Myr steps) of exhumation at rates of (b) 1.0 mm/yr, (c) 3.5 mm/yr, (d) 5.0 mm/yr, calculated with the program Thermod8 [*Hoisch*, 2005]; model thickness, 35 km; lower boundary condition, constant temperature; thermal diffusivity, 34.7 km^2 Myr^{-1}; thermal conductivity, 2.5 $J m^{-1} s^{-1} K^{-1}$; surface heat production, $1.67 \times E^{-10}$ $J m^{-1}$ s; length scale of heat production distribution, 10 km. Initial geothermal gradient is calculated from the same parameter set and a constant heat flow lower boundary condition of 42 $mW m^{-2}$. (e) 2D thermal model calculated with the program Thermod8 [*Hoisch*, 2005]; SPSZ hanging wall (right side).

erosion rates in the Alichur dome were similar to the northern Shakhdara dome. The lowest Miocene erosion rates occurred in the Turumtai horst and the southeastern Pamir (~0.2–0.4 mm/yr, see section 5.1).

5.4. Miocene Doming and Exhumation of the Shakhdara Dome Footwall

5.4.1. Cooling and Exhumation Rates

[32] The onset of doming at 21–20 Ma resulted in exhumation and cooling. The cooling path for the entire Shakhdara-Alichur crystalline rocks may be interpreted as continuous cooling from melt crystallization at ~750°C to upper crustal temperatures (~100°C) at a constant rate of ~40°C/Myr or, incorporating our titanite U-Pb data, as two stage, with early slow cooling followed by later rapid cooling (Figure 3). The cooling rates increase from the Shakhdara dome margins towards its interior: the highest rate is recorded in the deep core of the dome (Figure 7e, 6823C1: ~90°C/Myr); the high-elevation samples in the core cooled at ~50°C/Myr; the central parts of the dome record 35–75°C/Myr (Figure 7f). In the northern area of the dome (Figure 7 g), the cooling rates decrease from 30 to 40°C/Myr in the western part and at low elevations to ~10°C/Myr near the horst and at high elevations. Rapid cooling is also recorded along the SPSZ (30–70°C/Myr, Figure 7d). Although the precision of the calculated cooling rates is low, we propose that the distribution is significant and results, in part, from heat advection, which reduced cooling rates, especially at the onset of rapid exhumation. The cooling rates in the central and southern dome (~50–70°C/Myr) are thus closer to a dynamic thermal equilibrium than those in the northern part; they reflect earlier stages of doming.

[33] Recognizing the impact of advection and convection on calculating exhumation rates from cooling rates, we made first-order estimates based on (i) the pressure estimates for peak metamorphism in the Shakhdara dome (equivalent to 30–40 km of burial; *Schmidt et al*. [2011]) and ~20 Myr exhumation, and (ii) (equilibrium) geothermal gradients of ~40–60°C/km and cooling rates of 50–70°C/Myr; these yielded 1.5–2.0 and 0.8–1.8 mm/yr, respectively. The exhumation-rate estimates from cooling rates are higher if the thermal field had not reached dynamic equilibrium, or if geothermal gradients were lower than assumed. $^{40}Ar/^{39}Ar$, Rb-Sr, and ZHe age-elevation trends from the central and southern Shakhdara dome—less affected by isotherm advection than those from the northern dome—are ~0.2–1.0 mm/yr (Figures 8b–d); they are lower than the above estimates, but of the same order of magnitude (~1 mm/yr). Lower elevation trends of Wm and Bt $^{40}Ar/^{39}Ar$ and ZHe ages from the northern Shakhdara dome (0.2 and 0.5 mm/yr; Figure 8a) are consistent with rapid heat advection at the onset of tectonic exhumation.

[34] A more sophisticated approach to relate cooling to exhumation rates is afforded by the program Age2Edot [*Brandon et al*., 1998; *Ehlers et al*., 2005]. The program calculates the effect of the transient thermal field during exhumation on the closure temperature of a given thermochronometer, depth of closure isotherm, and cooling rate. The program employs a constant temperature lower boundary condition. The thermal parameters of our models (Figure 10a) were as follows: depth of constant temperature = 35 km; thermal diffusivity = 34.7 km^2/Myr; internal heat production = 8°C/Myr; surface temperature = 0°C; surface thermal gradient at no exhumation = 22°C/km. For a given exhumation rate, the cooling rate recorded by a high-temperature thermochronometer is predicted to be lower than that of a low-temperature thermochronometer. This is in agreement with our observations: where ZHe ages are available, they are younger than expected based on linear cooling trends (Figures 7d, 7f, and 7g), suggesting that cooling rates accelerated with time.

[35] An exhumation rate of 1 mm/yr corresponds to cooling rates of 18, 20 and 26°C/Myr for Wm, Bt $^{40}Ar/^{39}Ar$, and ZHe, respectively (Figure 10a). Conversely, $^{40}Ar/^{39}Ar$ to AFT cooling rates determined in the crystalline rocks away from the dome margins (~50–70°C/Myr; Figure 7d–f) correspond to exhumation at 1.5–3 mm /yr. The cooling rates determined in the Shakhdara crystalline rocks are thus inconsistent with (i.e., higher than) the exhumation rates determined from the age-elevation trends and the first-order estimates presented above; this conclusion is largely independent from the input parameters for the Age2Edot model. The discrepancy is possibly due to a transient thermal field or to low-temperature subvertical shortening (see section 3). We propose 1 and 3 mm/yr as minimum and maximum exhumation rates during Miocene doming (comprising tectonic and erosional exhumation).

5.4.2. Extension and Footwall Extrusion Rates

[36] The change from pro- to retrograde metamorphism, which we relate to the onset of doming, likely was early Miocene in the entire central and southern Pamir crust, given the ~21 Ma monazite and titanite U–Pb ages throughout the Shakhdara crystalline rocks [*Schmidt et al*., 2011]. The main exhumation and cooling of the Shakhdara dome was, however, diachronic. This is reflected in the southward younging cooling-age gradients of 0.1 Myr/km (Figures 9a and 9b) and is consistent with northward extrusion of the footwall along the low-angle SPSZ (Figure 2b).

[37] We use two approaches to assess horizontal tectonic rates: (i) An average value of~N-S extension is estimated from the width of the dome and the duration of doming. The ~90 km width of the dome and the ≤21 Myr maximum duration of doming yield a minimum extension rate of ~4 mm/yr for the Shakhdara dome. As we can exclude a

Figure 10. (caption continued) is fix, footwall exhumes as indicated by red arrows, red hatched bar illustrates successive exhumation of footwall. Results are represented by isotherms. Initial thermal gradient of 22°C/km as in Figures 10b–10d; detachment is modeled dipping 25° to the south and flattening at 35 km depth; slip rate is 10 mm/yr. Panels 2 to 5 illustrate the thermal field resulting from footwall exhumation after 2, 4, 10, and 20 Myr of doming; panels 6 and 7 thermal relaxation after 2 and 4 Myr of tectonic quiescence (no tectonic or erosional exhumation). Model thickness, 50 km; length, 221 km; thermal insulator lateral boundary conditions; constant heat flow lower boundary condition, 42 mW m^{-2}. (f) Evolution of the geothermal gradient at the trace of the South Pamir shear zone extracted from the model in Figure 10e. Initial gradient is ~22°C/km; during footwall exhumation the thermal gradient within the upper 5 km increases to 43°C/km after 4 Myr and 63°C/km after 20 Myr; relaxation reduces the gradient to 46 and 40°C/km within 2 and 4 Myr, respectively (blue lines).

significant component of coaxial ~N-S stretching at low temperatures from our structural observations [*Stübner et al.*, 2013], this extension rate is interpreted as a minimum slip rate along the SPSZ; with the end of doming at ~2 Ma, this value increases to ~5 mm/yr. (ii) A slip rate on the SPSZ is estimated from the cooling-age gradients. Interpreting the age gradients in Figures 9a and 9b (~10 mm/yr) in terms of extension or slip rate has caveats: erosion may lead to overestimation of the true rates if the erosion removed more material from the early exposed northern part of the dome than from the more recently exposed southern part. In section 5.3, we noted that erosion was higher along the dome axis (southern part of the dome) than in the northern part of the dome. Because of heat advection during doming, the geothermal gradient is expected to have increased from north to south; erosion is therefore expected to have had a stronger effect on cooling ages in the southern part of the dome, leading to an underestimation of the true extension rate. However, the total erosion of ≤2 km in the Shakhdara dome (see section 5.3) is insufficient to have a significant impact on ZHe, ZFT, or $^{40}Ar/^{39}Ar$ cooling ages.

[38] The effect of a changing geothermal field due to heat advection during doming on a N-S cooling-age gradient is twofold: (1) The geothermal gradient increases during doming, and as a result, cooling ages closer to the SPSZ are younger than they would be in the absence of heat advection; apparent extension rates determined from N-S age gradients consequently underestimate the true rate. (2) Advection of isotherms is most rapid at the onset of doming and subsequently decelerates. As discussed below, dynamic steady state may have been attained within several Myr. As a result, cooling ages recorded by low-temperature thermochronometers in the southern part of the dome are likely to be close to a dynamic equilibrium of the thermal field. Our data do not resolve a spatial variation in the N-S gradient or a significant difference between the thermochronometers (Figures 9a and 9b). We conclude that the effects of both variable erosion and heat advection during doming should underestimate the true extension rate by the age-distance relationships; this underestimation is, however, likely to be minor.

[39] Why then are the rates from the cooling age gradients (~10 mm/yr) higher than the estimates derived from the width of the dome and the duration of doming (~5 mm/yr)? We resolve this discrepancy by postulating that the early stages of doming and exhumation were accommodated by a mechanism different from top-to-SSE shear along the SPSZ and northward extrusion of its footwall. In this scenario, ~5 mm/yr reflects an average extension rate over the entire duration of doming, whereas ~10 mm/yr reflects the rate of footwall extrusion and ~N-S extension that characterized the second stage of dome formation. We suggest that doming started at 21–20 Ma by buckling of the southern Pamir crust and the onset exhumation of the northern Shakhdara dome along a top-to-NE normal fault zone. This normal fault zone either formed above a blind thrust, a splay of the reactivated Rushan-Pshart suture, or during bulk upper crustal extension of the central and northern southern Pamir due to the initiation and early rollback of the Pamir seismic zone (Figure 2c; *Sippl et al.* [2013]; *Rutte et al.* [2013]; *Stübner et al.* [2013]). This early stage of the GSZ evolution as a top-to-N normal fault zone initiated exhumation and cooling of the northern Shakhdara dome, as reflected by $^{40}Ar/^{39}Ar$ and Rb-Sr thermochronology. This stage of doming did not result in significant ~N-S extension in the southwestern Pamir, although a proto-SPSZ may have been active. Top-to-SSE flow and activation of the SPSZ as the major tectonic structure commenced several Myr later and resulted in the observed ~N-S age gradients of ~10 mm/yr; extrapolation of the trends in Figures 9a and 9b to the northern rim of the dome suggests that footwall extrusion began at ~18–15 Ma.

[40] Doming in the southwestern Pamir Shakhdara dome was thus characterized by an early Miocene stage of N-S buckling followed by rapid ~N-S extension and footwall exhumation along a low-angle detachment; footwall extrusion along the SPSZ did not occur until several Myr after the onset of doming. Calculations with the program RESPTIME [*Brandon et al.*, 1998; *Ehlers et al.*, 2005] (see also section 5.5) demonstrate that a change from background exhumation rates of 0.1 mm/yr (determined from the Turumtai horst and the southeastern Pamir, section 4) to high tectonic exhumation rates (simulated by exhumation rates ≤5 mm/yr) causes rapid heat advection that results in initially slow cooling rates; at the same time, closure temperatures for any given thermochronometer increase with time. The closure isotherm of ZHe, for example, is predicted to achieve quasi steady state (depth of closure isotherm changing by less than 0.2 mm/yr) within ~4 Myr after the instantaneous increase in exhumation rate; higher-temperature thermochronometers require longer to achieve quasi steady-state (e.g., $^{40}Ar/^{39}Ar$: ~5–6 Myr). Near-steady state is approached slightly faster for lower exhumation rates, e.g., 3–5 Myr for an exhumation rate of 1 mm/yr. These calculations suggest that a dynamic equilibrium may have been attained within a few Myr after the onset of doming, and that heat advection may not have influenced the apparent extension rate of ~10 mm/yr obtained from the ZHe ages significantly; the ZHe age gradient may thus be a good first-order estimate of the true slip rate along the SPSZ.

[41] Along the southern dome margin, the SPSZ dips 20–30°—locally steeper—to the southeast [*Stübner et al.*, 2013]. Extrapolating the dip of 20–30° to depth, the slip rate of 10 mm/yr translates to a tectonic exhumation rate of 3.5–5 mm/yr. An exhumation depth of ~45–80 km, calculated from these rates and the ~13–16 Myr duration of extension (onset at ~18–15 Ma, end at ~2 Ma), exceeds the petrologically determined maximum depths of 30–40 km [*Schmidt et al.*, 2011], and we surmise that a subhorizontal detachment in the middle crust limited the maximum exhumation depth. With a listric shear-zone geometry that flattens at ~35 km depth, exhumation rates vary as a function of depth; higher-temperature thermochronometers are predicted to trace lower exhumation rates than lower-temperature thermochronometers, and the above estimate of 3.5–5 mm /yr must be considered as an upper limit of the rates of tectonic exhumation. This is in agreement with the exhumation rates calculated from cooling rates (1.5–3 mm /yr, section 5.4.1); lower rates determined from age-elevation trends (0.2–1.0 mm/yr) may correspond to exhumation rates at greater depths reflecting flattening of the detachment.

5.5. Doming and Heat Advection

[42] We used the program Thermod8, v.2.3 [*Hoisch*, 2005] to explore the thermal evolution of the crust during doming. The models are intended as first-order approximations: uncertainties include approximation of thermal parameters by

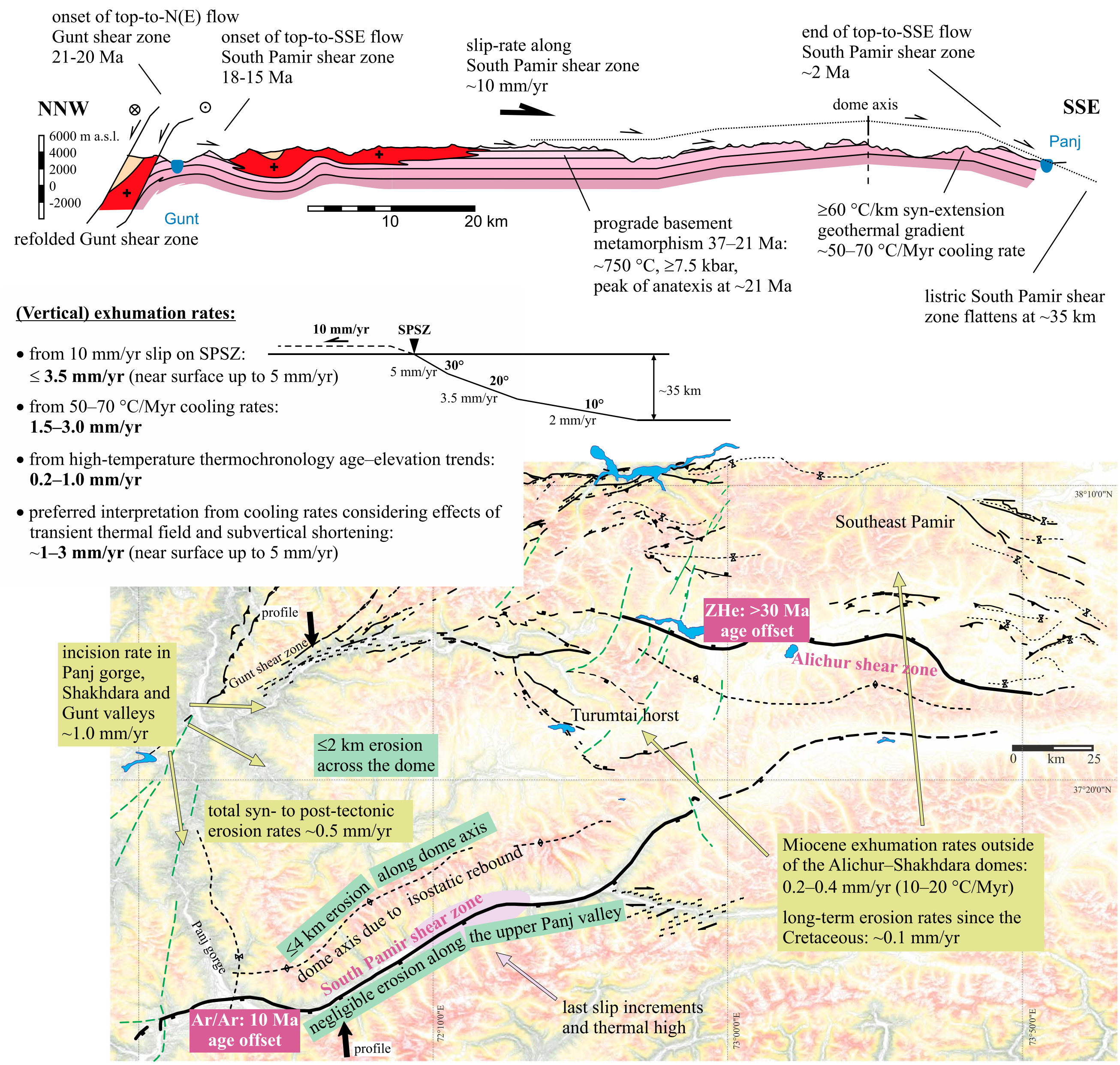

Figure 11. Overview of timing and rates of gneiss-dome formation in the southwestern Pamir.

average values [*Hoisch*, 2005; *Ehlers*, 2005] and assumptions about fault geometry (dip angle, detachment depth) and kinematics (slip rate; see discussion above); erosional exhumation is not incorporated in the models. The purpose of the models is to explore the temporal and spatial variability of the near-surface geothermal gradients, which is essential for evaluation of low-temperature thermochronometer data.

[43] Thermod8 allows 1D and 2D calculations of heat conduction and advection in response to exhumation and faulting. For 1D calculations, the input parameters are thermal diffusivity, effective thermal diffusivity for molten rocks, solidus temperature, initial geothermal gradient, heat production, and thermal conductivity; all parameters may vary with depth. The lower boundary condition is either constant temperature or constant heat flux. We first calculated a stable geothermal gradient after *Turcotte and Schubert* [2002] for a basal heat flow of 42 $mW\,m^{-1}$, thermal diffusivity of 34.7 $km^2\ Myr^{-1}$, thermal conductivity of 2.5 $J\,m^{-1}\,s^{-1}\,K^{-1}$, surface heat production of $1.67 \times E^{-10}\,J\,m^{-1}\,s^{-1}$, and a length scale of 10 km; this parameter set corresponds to that of the Age2Edot model in Figure 10a. In order to simulate a subhorizontal detachment at ~35 km depth, as postulated above, we set up a 35 km thick model with a constant temperature lower boundary condition; exhumation rates were 1.0, 3.5, and 5.0 mm/yr (Figures 10b–d). In agreement with the estimates obtained from RESPTIME (see above), a dynamic equilibrium was attained within ~5 Myr. Near-surface geothermal gradients in the upper 5 km of the crust changed from the initial 22°C/km to 28, 53, and 67°C/km at steady-state (Figures 10b–d). No reliable surface heat-flow measurements or estimates of the near-surface geothermal gradient are available for the Pamir [http://www.heatflow.und.edu/index.html], but the abundance of hot springs in the southwestern Pamir (Figure 2a in *Stübner et al.* [2013]) suggests that thermal

gradients are high today and may well have been as high as 45–60°C/km in the Miocene.

[44] Figures 10e and f show results of a 2D Thermod8 model of footwall exhumation, in which the SPSZ dips 25° and flattens at 35 km depth; the assumed slip rate was 10 mm/yr, corresponding to a rock uplift rate of 4.7 mm/yr, and the lower boundary condition was a constant heat flow of 42 mW m^{-2}. At the trace of the SPSZ, the thermal gradient within the upper 5 km of the crust increases from an initial value of 22°C/km to 43°C/km after 4 Myr and 63°C/km after 20 Myr, comparable to the predictions of the 1D model (exhumation rate of 5.0 mm/yr; Figure 10d). Figure 10e illustrates the N-S variation of the thermal field: after 10 Myr of footwall exhumation, the near-surface thermal gradient is 59°C/km at the fault trace; in the hanging wall, 5 km south of the SPSZ, it is 53°C/km; and at the northern dome margin, 90 km north of the SPSZ, the thermal gradient is 27°C/km. The lower two panels of Figure 10e illustrate thermal relaxation 2 and 4 Myr after the end of doming. At the trace of the SPSZ, the near-surface thermal gradients relax to ≤46°C/km within 2 Myr, and ≤40°C/km within 4 Myr of tectonic quiescence (Figures 10e, f). These models demonstrate the spatial and temporal variability of the geothermal gradient. At the end of doming, geothermal gradients in the southern Shakhdara dome may have exceeded 60 °C/km; in the northern dome and in the hanging wall, geothermal gradients were significantly lower. Relaxation since the end of tectonic exhumation may have reduced gradients to ≤40–45°C/km.

6. Conclusions

[45] Gravitational collapse of thick Cenozoic Pamir crust resulted in the formation of large extensional gneiss domes in the Pamir; the largest of which is the ~350 × 90 km composite Shakhdara-Alichur gneiss dome of the southern Pamir. *Stübner et al*. [2013] established a kinematic model of dome formation under N-S extension accommodated by two low-angle, normal-shear detachment faults, the SPSZ and the ASZ. A comprehensive geo-thermochronologic data set of titanite, zircon, and monazite U/Th-Pb, mica Rb-Sr and $^{40}Ar/^{39}Ar$, ZFT, ZHe, and AFT ages from crystalline rocks of the SPSZ and ASZ footwalls, the low-strain Turumtai horst that separates the Shakhdara from the Alichur dome, and the hanging walls, together with 1D and 2D thermal models, constrain the onset and end of ~N-S extension in the southwestern Pamir, vertical and horizontal tectonic rates, and erosion rates. The principal results are summarized in Figure 11 and are as follows:

[46] 1. Doming started at 21–20 Ma and subsequently resulted in exhumation of high-grade metamorphic (~750° C, ≥7.5 kbar) and migmatitic rocks in the Shakhdara dome. The early stages of doming triggered the activation of the Gunt shear zone (GSZ) as a top-to-N(E) normal-shear zone.

[47] 2. The bulk of the Shakhdara dome was exhumed by top-to-SSE ductile flow along the SPSZ, starting at ~18–15 Ma and accounting for up to 90 km N-S extension in the southern Pamir. The slip rate along the SPSZ was ~10 mm/yr, corresponding to exhumation rates of ~1–5 mm /yr, depending on the dip angle of the detachment. We propose a listric shear-zone geometry with flattening at midcrustal depth (~35 km). ~N-S extension was coeval with ongoing ~N-S convergence between India and Asia, and deformation in the Pamir was spatially partitioned into extensional dome formation and shortening and crustal thickening. We suggest that gravitational collapse of thickened southwestern Pamir crust was the driving mechanism for doming and upper-middle crustal extension; this collapse drove shortening, in particular in its northwestern foreland, the Tajik depression fold-and-thrust belt ("vertical extrusion" scenario [*Stübner et al*., 2013]). Doming and ~N-S extension ended at ~2 Ma.

[48] 3. Bulk erosion within the Shakhdara dome is less than ~2 km. Low erosion rates preserved most of the ≤4 km thick SPSZ, which comprises nearly all of the exposure of the Shakhdara dome; footwall rocks crop out in the deeply incised Panj gorge. Erosion along the southern dome margin (SW-flowing Panj) is negligible. Syn- to post-tectonic erosion rates have been on the order of 0.5 mm/yr and varied spatially with the highest rates along the dome axis. Incision within the major drainages (Panj gorge, Shakhdara river valley) was ~1.0 mm/yr.

[49] 4. The Alichur dome formed about contemporaneously with the Shakhdara dome by top-to-N flow along the ASZ. Exhumation depths are less (10–20 km) than in the Shakhdara dome; the onset and end of doming are poorly constrained yet. Miocene exhumation rates in the Turumtai horst and in the SE Pamir are low (0.2–0.4 mm/yr) and close to long-term, Cretaceous to Cenozoic rates of ~0.1 mm/yr.

[50] 5. Thermal models reconcile recorded cooling rates and age-elevation trends and illustrate the spatial and temporal variability of geothermal gradients. Geothermal gradients in the southern Shakhdara dome may have exceeded 60°C/km at the end of doming; in the northern Shakhdara dome and in the hanging wall, geothermal gradients were significantly lower. Since the end of tectonic exhumation at ~2 Ma, thermal gradients may have relaxed to ≤40–45°C/km.

[51] 6. In part 1 of this paper series [*Stübner et al*., 2013], we compared the vertical extrusion scenario of the Shakhdara-Alichur gneiss domes outlined by structural observations to the extrusion of the Greater Himalayan crystalline basement rocks of the Himalaya. The main difference between the Pamir and the Himalaya is the intense erosion of the Greater Himalayan crystalline rocks, which is in contrast to negligible erosion affecting the Pamir gneiss domes; this is an effect of a drastically different climatic scenario, with the Himalaya dominated by the Monsoon and the Pamir by the Westerlies. The formation of the North Himalayan gneiss domes, on the other hand, has at least in part been attributed to diapiric ascent of partially molten rock (pronounced granitic cores, significant vertical thinning; [e.g., *Lee et al*., 2004]); this mechanism does not play a role in the southwestern Pamir domes [*Stübner et al*., 2013].

Appendix A

A1. Sample Processing

[52] Sample preparation and mineral separation were carried out at the TU Bergakademie Freiberg: samples were fragmented by high-voltage discharge employing a SELFRAG® facility [specifications http://selfrag.com] or a jaw crusher and sieved. Minerals were concentrated by standard mineral separation procedures (magnetic separation, tetrabromethane, and diiodmethane heavy liquids) and further refined by handpicking.

A2. Rb-Sr Geochronology

[53] The isotope dilution-TIMS work for Rb-Sr was done at TU Bergakademie Freiberg. Samples were weighed into Savillex screw-top containers, spiked, and dissolved in a mixture of HF and HNO_3. Solutions were processed by standard cation-exchange techniques. Isotope measurements were carried out on a Finnigan MAT 262 mass spectrometer. Sr measurements were done by static multicollection. Precision of Rb and Sr concentrations—determined on repeated analyses of the USGS whole rock standards GSP-2 and BCR-2—is estimated at about 1%, precision of $^{87}Sr/^{86}Sr$ isotope ratios is ≤0.02%. The value obtained for the $^{87}Sr/^{86}Sr$ ratio of the NBS standard SRM 987 during the period of analytical work was 0.710288 ± 0.000038 (n = 23). Rb and Sr blanks were <200 pg and are insignificant for the mineral weights used. We used the program ISOPLOT [*Ludwig*, 2008] for isochron calculation; errors are reported at the 2σ level.

A3. $^{40}Ar/^{39}Ar$ Thermochronology

[54] $^{40}Ar/^{39}Ar$ analysis was carried out at three different laboratories: Stanford University, USA, the SEAL laboratory of the Slovak Academy of Sciences, Bratislava, Slovakia, and the ALF laboratory at TU Bergakademie Freiberg, Germany. Analytical procedures for the Stanford laboratory were similar to those reported in *Hacker et al*. [1996]. In short, the minerals were cleaned by ultrasound, rinsed in acetone, isopropyl alcohol, and distilled water, packaged in pure Cu foil, stacked in SiO_2 vials together with neutron fluence monitors, and irradiated at the Oregon State University TRIGA reactor. We used Taylor Creek sanidine (USGS standard 85G003; *Duffield and Dalrymple* [1990]) with an assigned age of 27.92 ± 0.17 Ma as a neutron fluence monitor. The grains were heated under UHV conditions in a double-vacuum Staudacher-type resistance furnace. The evolved gas was purified during extraction by SAES ST-172 and ST-101 getters and a stainless steel cold finger and was analyzed on a MAP 216 mass spectrometer fitted with a Baur-Signer ion source and a Johnston MM1 multiplier with a sensitivity of approximately 2×10^{-14} mol/V. Analyses were corrected for system blanks and instrumental mass discrimination using the program EyeSoreCon written by B. R. Hacker.

[55] Analytical procedures for the SEAL laboratory were similar to those reported in *Frimmel and Frank* [1998]; this paper includes details regarding corrections for mass discrimination and radioactive decay, as well as for the determination of the J-value and the definition of a plateau age. Mineral concentrates were enclosed in high-purity quartz vials and irradiated at the nuclear research reactor VR-1 in Prague, Czech Republic. The samples were filled into annealed Ta capsules and subsequently analyzed by stepwise heating experiments.

[56] The ALF laboratory at the TU Bergakademie Freiberg is a new facility [*Pfänder et al*., 2010], and thus we provide a more detailed description in the following. Mineral separates were repeatedly ultrasonicated in alcohol and de-ionized water, dried, and subsequently wrapped into Al foil. The Al-sample packets were loaded in 5 × 5 mm wells on 33 mm Al-discs for irradiation, which was done under Cd shielding at the FRG II reactor in Geesthacht, Germany, at a thermal neutron fluence of $\sim 5 \times 10^{13}$ n/cm^{2}s and a thermal to fast neutron ratio of ~40. Irradiated samples were unwrapped and loaded in 3 × 1 mm (diameter × depth) wells on an oxygen free copper disc for measurements. Step heating was performed using an energy controlled floating 30 W CO_2 laser system at 10.6 μm wavelength with a defocused beam of 3 mm diameter, followed by gas purification applying two AP10N getter pumps, one at room temperature and one at 400°C. Laser heating time was 5 min; cleaning time was 10 min per step. Ar isotope compositions were measured in static mode using a GV Instruments ARGUS noble gas mass spectrometer equipped with five Faraday cups and 10^{12} ohm resistors on mass positions 36–39 and a 10^{11} ohm resistor on mass position 40. Typical blank levels are 2.5×10^{-16} mol ^{40}Ar and 8.1×10^{-18} mol ^{36}Ar. Measurement time was 7.5 min per step acquiring 45 scans at 10 s integration time each. Mass bias was corrected assuming linear mass-dependent fractionation and using an atmospheric $^{40}Ar/^{36}Ar$ ratio of 295.5. For raw data reduction, an in-house developed MATLAB toolbox was used; isochron, inverse isochron, and plateau ages were calculated using ISOPLOT [*Ludwig*, 2008]. All ages were calculated using Fish Canyon sanidine as a flux monitor (28.305 ± 0.036 Ma; *Renne et al*. [2010]); errors on ages are 2σ. Corrections for interfering Ar isotopes were done using $(^{36}Ar/^{37}Ar)_{Ca} = 0.000261$, $(^{39}Ar/^{37}Ar)_{Ca} = 0.000709$, $(^{38}Ar/^{39}Ar)_K = 0.0107$, and $(^{40}Ar/^{39}Ar)_K = 0.0024$ and applying 5% uncertainty. Ar-Ar isotope-correlation diagrams are presented only for those samples that appear to contain excess ^{40}Ar, as indicated by systematically discordant (e.g., saddle-shaped) age spectra and/or nonatmospheric $^{40}Ar/^{36}Ar$ intercepts. The uncertainties quoted for the $^{40}Ar/^{39}Ar$ dates do not include the ~1% uncertainty in monitor ages and/or decay constants [*Renne et al*., 2010].

[57] Closure temperatures [*Dodson*, 1973] for white mica (Wm) and biotite (Bt) were calculated with the program CLOSURE [*Brandon et al*., 1998], based on the diffusion parameters of *Grove and Harrison* [1996] (Bt), and *Robbins* [1972] and *Hames and Bowring* [1994] (Wm). Cooling rates for closure-temperature estimation were determined from multiple thermochronometers. For rapidly cooled crystalline-rock samples, we obtained closure temperatures of ~360–380°C (Bt) and ~400–420°C (Wm); for the more slowly cooled rocks, e.g., in the hanging wall of the SPSZ, we obtained closure temperatures of 330–340°C (Bt) and 360–380°C (Wm). Grain-size variation was not considered; instead, a volume-to-area ratio of 250 μm was assumed for all samples. We assigned an error of ±20°C to the closure temperatures.

A4. Fission Track and (U-Th)/He Dating

[58] Apatite and zircon mineral concentrates for fission track and (U-Th)/He dating were obtained from the sieved 63–125 μm grain-size fraction. For apatite fission track dating (AFT), grains were mounted in epoxy resin, ground, and polished. Fossil tracks were etched at 25°C in 23% HNO_3 for 15 s. Mounts were covered with Goodfellow muscovite as external detector and irradiated in five batches at the research reactors of TU München (FG10, FG16, FG17, FG20, FG25, and FG54) or Oregon State University (Goe112). With each irradiation, we included three mounts of Durango apatite as age standard and IRMM-540R (FG10-54) or CN5 (Goe112) glass to monitor neutron

fluence; the obtained induced glass track densities were piecewise linearly extrapolated to the location of each mount within the irradiation (Table 4, ρ_d). Induced tracks in the external detector were etched at 23°C in 40% HF for 40 min. Fossil and induced track densities were counted with a Zeiss Axioplan microscope using the repositioning technique of *Jonckheere et al.* [2003]. Counting was carried out by three operators using 500× or 1000× magnification; the calibration factor for each AFT ζ-age is reported in Table 4. Track counting was hampered by generally low track densities and low and inhomogeneous U distributions; several samples have distinct high-U rims. We report pooled AFT ζ-ages calculated from total induced and spontaneous track numbers (N_i, N_s), which are based on counts of typically 20–60 individual areas within the mount. If more than one mount was prepared for one sample, we used the weighted mean of the single mount ages; errors on sample ages are reported at the 1σ level. We used CLOSURE [*Brandon et al.*, 1998] to calculate an effective closure temperature for each sample from the cooling rates determined from multiple thermochronometers and assuming an average apatite composition [*Ketcham et al.*, 1999]. For most samples, this procedure resulted in an AFT closure temperature of 120 ± 10°C.

[59] Zircon fission track ages were obtained by the ζ- and Z-calibration methods using the Fish Canyon tuff and Tardree rhyolite age standards and the IRMM-541 standard uranium glass. Zircons were embedded in PFA Teflon® at 320°C. For easier grinding and polishing, we encase the Teflon mount in epoxy. After removal of the Teflon mount from the epoxy, the mount was stepwise etched with a 7:5 mixture of eutectic melt of NaOH and KOH at 228°C for 0.5 to 17 h. 50 μm thick external detector Goodfellow muscovites were attached to the etched zircon and unetched IRMM-541 mounts. The zircon, age standards, and IRMM-541 mounts were irradiated (FG38) together at the SCK.CEN reactor in Mol, Belgium. The external detectors were etched 30 min in 48% HF at room temperature. Mounts, and the corresponding external detectors were fixed side-by-side, track-side up on glass slides and tracks were counted at a nominal magnification of 1250× in the external detector and IRMM-541 glass, and 2500× in the zircons mounts using a Zeiss Axioplan microscope equipped with an Autoscan® stage. For zircon fission track, CLOSURE calculations, based on the fanning model of *Tagami et al.* [1998], yielded closure temperatures of 327–358°C.

[60] Zircon (U-Th)/He dating (ZHe) was conducted at the Geochronology Center Göttingen. For each sample, three to four single, unbroken, idiomorphic crystals with similar size, shape, and color were selected and documented by digital photographs. Single-grain aliquots were degassed by a diode laser and He contents were measured with a Hiden triple-filter quadrupole mass spectrometer. For actinide determination, single-grain aliquots were unwrapped from Pt capsules, spiked with a calibrated ^{233}U-^{230}Th solution, and dissolved in pressurized Teflon bombs over 5 days using a HF-HNO_3 mixture. An Elan DRC ICP-MS equipped with an APEX microflow nebulizer was used for measuring the actinide, Sm, and Zr concentrations. Alpha-ejection correction (F_T-factor) was calculated following *Hourigan et al.* [2005] based on idealized dipyramidal prism grain geometry. Sample ages are unweighted means of single-grain ages; errors are 2σ. We calculated ZHe closure temperatures for each sample from He-in-zircon diffusion parameters [*Reiners et al.*, 2004] and average grain dimensions (Table 3) using CLOSURE [*Brandon et al.*, 1998]; they span 173–214°C.

A 5. Analytical Details for U-Pb Titanite LA-MC-ICP-MS at UCSB

[61] The analyses at UCSB were conducted using a Nu Instruments Plasma MC-ICP-MS and a Photon Machines 193 nm ArF excimer laser ablation system; details are given in *Spencer et al.* [2013]. The titanite analyses were conducted for 30 s each using a 30–40 μm diameter spot, a frequency of 4 Hz, and an energy of 3 mJ (equating to crater depths of ~10 μm). Primary reference material BLR-1 titanite (1047.4 ± 0.4 Ma $^{206}Pb/^{238}U$ ID-TIMS age) [*Aleinikoff et al.*, 2007] was employed to monitor and correct for mass bias and Pb/U fractionation. To monitor accuracy, secondary reference titanite Y17501C5 (385.8 ± 0.8 Ma ID-TIMS and ICP U-Pb isochron age) was analyzed every four unknowns. Data reduction was carried out using Iolite [*v*]. The overall uncertainty achieved on the U-Pb, Pb-Pb, and Th-Pb ages of the secondary reference materials throughout the instrument lifetime is 2% (2σ).

[62] **Acknowledgments.** TIPAGE field team members are I. Bahram, M. Gadoev, R. Gloaguen, R. Jonckheere, E. Kanaev, V. Minaev, I. Oimahmadoc, N. Rajabov, and K. P. Stanek. This research was funded by the DFG bundle TIPAGE (PAK 443), in particular RA 442/34, the bundle CAME, subproject TIPTIMON, funded by the German Federal Ministry of Education and Research (support code 03G0809), US National Science Foundation grant EAR-0838269, and the University of California. KS received support from the Studienstiftung des Deutschen Volkes. All fieldwork participants benefited from DAAD travel grants. JC acknowledges the RISE program of the DAAD that allowed her AFT work at Freiberg. Work in Tajikistan and Afghanistan would have been impossible without the continuous support of the Tajik Academy of Sciences, in particular its president M.I. Ilolov, and Focus Humanitarian Assistance, an affiliate of the Aga Khan Development Network. We thank the entire TIPAGE group (GFZ Potsdam, Universität Jena, TU Bergakademie Freiberg) for fascinating discussions and support. The manuscript benefited from reviews by M. Hubbard and J. Van Den Driessche.

References

Aleinikoff, J. N., R. P. Wintsch, R. P. Tollo, D. M. Unruh, C. M. Fanning, and M. D. Schmitz (2007), Ages and origins of rocks of the Killingworth Dome, south-central Connecticut; implications for the tectonic evolution of southern New England, *Am. J. Sci.*, *307*, 63–118.

Brandon, M. T., M. K. Roden-Tice, and J. I. Garver (1998), Late Cenozoic exhumation of the Cascadia accretionary wedge in the Olympic Mountains, northwest Washington State, *Geol. Soc. Am. Bull.*, *110*, 985–1009, doi:10.1130/0016-7606(1998)110<0985:LCEOTC>2.3.CO;2.

Brunel, M., N. Arnaud, P. Tapponnier, Y. Pan, and Y. Wang (1994), Kongur Shan normal fault: Type example of mountain building assisted by extension (Karakoram fault, eastern Pamir), *Geology*, *22*, 707–710.

Buchroithner, M. F. (1980), An outline of the geology of the Afghan Pamirs, *Tectonophysics*, *62*, 13–35.

Dodson, M. H. (1973), Closure temperature in cooling geochronological and petrological systems, *Contrib. Mineral. Petrol.*, *40*, 259–274.

Doebrich, J. L. and R. R. Wahl (Compilators) (2006), Geological and mineral resource map of Afghanistan; Version 2, *U.S. Geol. Surv. Open File Rep., 2006-1038*.

Duffield, W. A., and G. B. Dalrymple (1990), The Taylor Creek Rhyolite of New Mexico: A rapidly emplaced field of lava domes and flows, *Bull. Volcanol.*, *52*, 475–487.

Ehlers, T. (2005), Crustal thermal processes and the interpretation of thermochronometer data, *Rev. Min. Geochem.*, *58*, 315–350, doi:10.2138/rmg.2005.58.12.

Ehlers, T. A., T. Chaudhri, S. Kumar, C. W. Fuller, S. D. Willett, R. A. Ketcham, and M. T. Brandon (2005), Computational tools for low-temperature thermochronometer interpretation, *Rev. Min. Geochem.*, *58*, 589–622, doi:10.2138/rmg.2005.58.22.

Farley, K. A., R. A. Wolf, and L. T. Silver. (1996), The effects of long alpha-stopping distances on (U-Th)/He ages, *Geochim. Cosmochim. Acta*, *60*, 4223–4229, doi:10.1016/S0016-7037(96)00193-7.
Frimmel, H. E., and W. Frank (1998), Neoproterozoic tectono-thermal evolution of the Gariep Belt and its basement, Namibia/SouthAfrica, *Precambrian Res.*, *90*, 1–28.
Grew, E. S., N. N. Pertsev, M. G. Yates, A. G. Christy, N. Marquez, and J. V. Chernosky (1994), Sapphirine + forsterite and sapphirine + humite-group minerals in an ultra-magnesian lens from Kuhi-lal, SW Pamirs, Tajikistan: Are these assemblages forbidden?, *J. Petrol.*, *35*, 1275–1293.
Grove, M., and T. M. Harrison (1996), ^{40}Ar* diffusion in Fe-rich biotite, *Am. Mineral.*, *81*, 940–951.
Hacker, B. R., J. L. Modenfelder, and E. Gnos (1996), Rapid emplacement of the Oman ophiolite: Thermal and geochronologic constraints, *Tectonics*, *15*, 1230–1247.
Hacker, B. R., P. Luffi, V. Lutkov, V. Minaev, L. Ratschbacher, T. Plank, M. Ducea, A. E. Patiño-Douce, M. O. McWilliams, and J. Metcalf (2005), Near-ultrahigh pressure processing of continental crust: Miocene crustal xenoliths from the Pamir, *J. Petrol.*, *46*, 1661–1687.
Hames, W. E., and S. A. Bowring (1994), An empirical evaluation of the argon diffusion geometry in muscovite, *Earth Planet. Sci. Lett.*, *124*, 161–169, doi:10.1016/0012-821X(94)00079-4.
Hoisch, T. D. (2005), THERMOD7: A general two-dimensional numerical modeling program for heat conduction and advection, with special application to faults, *Comput. Geosci.*, *31*, 698–703.
Hourigan, J. K., P. W. Reiners, and M. T. Brandon (2005), U-Th zonation-dependent alpha-ejection in (U-Th)/He chronometry, *Geochim. Cosmochim. Acta*, *69*, 3349–3365, doi:10.1016/j.gca.2005.01.024.
Hubbard, M. S., E. S. Grew, K. V. Hodges, M. G. Yates, and N. N. Pertsev (1999), Neogene cooling and exhumation of upper-amphibolite-facies 'whiteschists' in the southwest Pamir Mountains, Tajikistan, *Tectonophysics*, *305*, 325–337.
Jenkin, G. R. T. (1997), Do cooling paths derived from mica Rb-Sr data reflect true cooling paths?, *Geology*, *25*(10), 907–910.
Jonckheere, R., L. Ratschbacher, and G. A. Wagner (2003), A repositioning technique for counting induced fission-tracks in muscovite external detectors in single-grain dating of minerals with low and inhomogeneous uranium concentrations, *Radiat. Meas.*, *37*, 217–219.
Kelsey, D. E., C. Clark, and M. Hand (2008), Thermobarometric modelling of zircon and monazite growth in melt-bearing systems: Examples using model metapelitic and metapsammitic granulites, *J. Metam. Geol.*, *26*, 199–212, doi:10.1111/j.1525-1314.2007.00757.x.
Ketcham, R. A., R. A. Donelick, and W. D. Carlson (1999), Variability of apatite fission-track annealing kinetics: III. Extrapolation to geological time scales, *Am. Min.*, *84*, 1235–1255.
Lee, J., B. R. Hacker, and Y. Wang (2004), Evolution of North Himalayan gneiss domes: Structural and metamorphic studies in Mabja Dome, southern Tibet, *J. Struct. Geol.*, *26*(12), 2297–2316, doi:10.1016/j.jsg.2004.02.013.
Ludwig, K. R. (2008), Isoplot 3.70. A geochronological toolkit for Microsoft Excel, *Berkeley Geochronol. Cent. Spec. Publ., 4*, 1–76.
Mechie, J., et al. (2012), Crustal and uppermost mantle velocity structure along a profile across the Pamir and southern Tien Shan as derived from project TIPAGE wide-angle seismic data, *Geophys. J. Int.*, *188*, 385–407, doi:10.1111/j.1365-246X.2011.05278.x.
Paton, C., J. D. Woodhead, J. C. Hellstrom, J. M. Hergt, A. Greig, and R. Maas (2010), Improved laser ablation U-Pb zircon geochronology through robust downhole fractionation correction, *Geochem. Geophys. Geosyst.*, *11*, Q0AA07, doi:10.1029/2009GC002618.
Pfänder, J., B. Sperner, and L. Ratschbacher (2010), The new Ar-Ar geochronology facility at Freiberg, Germany: Instrumentation, applications, and current limitations, *Geophys. Res. Abstr.*, *12*, EGU2010-5496.
Reiners, P. W., T. L. Spell, S. Nicolescu, and K. A. Zanetti (2004), Zircon (U-Th)/He thermochronometry: He diffusion and comparisons with ^{40}Ar/^{39}Ar dating, *Geochim. Cosmochim. Acta*, *68*, 1857–1887, doi:10.1016/j.gca.2003.10.021.
Renne, P. R., R. Mundil, G. Balco, K. Min, and K. R. Ludwig (2010), Joint determination of ^{40}K decay constants and ^{40}Ar*/^{40}K for the Fish Canyon sanidine standard, and improved accuracy for ^{40}Ar/^{39}Ar geochronology, *Geochim. Cosmochim. Acta*, *74*, 5349–5367.
Robbins, G. A. (1972), Radiogenic argon diffusion in muscovite under hydrothermal conditions, M.S. Thesis, Brown Univ., Providence, R.I., 42 pp.
Robinson, A. C., A. Yin, C. E. Manning, T. M. Harrison, S. H. Zhang, and X. F. Wang (2004), Tectonic evolution of the northeastern Pamir: Constraints from the northern portion of the Cenozoic Kongur Shan extensional system, western China, *Geol. Soc. Am. Bull.*, *116*, 953–973, doi:10.1130/B25375.1.
Robinson, A. C., A. Yin, C. E. Manning, T. M. Harrison, S. H. Zhang, and X. F. Wang (2007), Cenozoic evolution of the eastern Pamir: Implications for strain-accommodation mechanisms at the western end of the Himalayan-Tibetan orogen, *Geol. Soc. Am. Bull.*, *119*, 882–896, doi:10.1130/B25981.1.
Rutte, D., M. Stearns, and L. Ratschbacher (2013), The eastern Central Pamir Gneiss Domes: Temporal and spatial geometry of burial and exhumation, *Geophys. Res. Abstr.*, *15*, EGU2013-6090.
Schmidt, J., B. R. Hacker, L. Ratschbacher, K. Stübner, M. Stearns, A. Kylander-Clark, J. M. Cottle, A. Webb, G. Gehrels, and V. Minaev (2011), Cenozoic deep crust in the Pamir, *Earth Planet. Sci. Lett.*, *312*, 411–421, doi:10.1016/j.epsl.2011.10.034.
Schwab, M. (2004), The amalgamation of the Pamirs and their subsequent evolution in the far field of the India–Asia collision, Doctoral thesis, Univ. of Tübingen, Tübingen, Germany, 185 pp.
Schwab, M., et al. (2004), Assembly of the Pamirs: Age and origin of magmatic belts from the southern Tien Shan to the southern Pamirs and their relation to Tibet, *Tectonics*, *23*, TC4002, doi:10.1029/2003TC001583.
Seydoux-Guillaume, A. M., J. L. Paquette, M. Wiedenbeck, J. M. Montel, and W. Heinrich (2002), Experimental resetting of the U–Th–Pb systems in monazite, *Chem. Geol.*, *191*, 165–81.
Sippl, C., et al. (2013), Geometry of the Pamir–Hindu Kush intermediate-depth earthquakes zone from local seismic data, *J. Geophys. Res. Solid Earth*, *118*, 1438–1457, doi:10.1002/jgrb.50128.
Smit, M. A., B. R. Hacker, and L. Ratschbacher (2012), Lu–Hf geochronology constrains slow burial of crust in active orogens: The Pamir gneiss domes, *Eur. Mineral. Conf., 1*, EMC2012-706.
Spencer, K., B. R. Hacker, A. R. C. Kylander-Clark, T. B. Andersen, J. M. Cottle, M. A. Stearns, J. E. Poletti, and G. G. E. Seward (2013), Campaign-style titanite U-Pb dating by ICP: Implications for crustal flow, phase transformations and titanite closure, *Chem. Geol.*, *341*, 84–101, doi:10.1016/j.chemgeo.2012.11.012.
Strecker, M. R., W. Frisch, M. W. Hamburger, L. Ratschbacher, S. Semiletkin, A. Zamoruyev, and N. Sturchio (1995), Quaternary deformation in the eastern Pamirs, Tadzhikistan and Kyrgyzstan, *Tectonics*, *14*, 1061–1079.
Stübner, K., et al. (2013), The giant Shakhdara migmatitic gneiss dome, Pamir, India–Asia collision zone: 1. Geometry and kinematics, *Tectonics*, doi:10.1002/tect.20057, in press.
Tagami, T., R. F. Galbraith, R. Yamada, and G. M. Laslett (1998), Revised annealing kinetics of fission tracks in zircon and geologic implications, in *Advances in Fission-Track Geochronology*, Kluwer Acad., Dordrecht, Netherlands, pp. 99–204.
Turcotte, D. L., and G. Schubert (2002), *Geodynamics*, Cambridge Univ. Press, Cambridge, UK.
Vermeesch, P. (2012), On the visualization of detrital age distributions, *Chem. Geol.*, *312–313*, 190–194, doi:10.1016/j.chemgeo.2012.04.021.
Vlasov, N. G., Y. A. Dyakov, and E. S. Cherev (Eds) (1991), *Geological Map of the Tajik SSR and Adjacent Territories, 1:500,000*, Vsesojuznoi Geol., Inst., Leningrad, Russia.